buildings

MDPI

Article

Blast Resistance of RC Slabs Strengthened with Concrete-Based Protective Layers Under Contact Explosion

Meili Meng [1], Shubo Dai [1], Jinlei Zheng [2,3], Ran Song [4,5], Kelei Cao [1,*] and Changhui Zhang [1]

[1] School of Water Conservancy, North China University of Water Resources and Electric Power, Zhengzhou 450046, China; mengmeili@ncwu.edu.cn (M.M.); dai15226065347@163.com (S.D.); zhangchanghui@ncwu.edu.cn (C.Z.)
[2] Henan Railway Construction and Investment Group Limited Company, Zhengzhou 450000, China; zhengjinlei@yeah.net
[3] Henan New Infrastructure of Railway Construction Investment Limited Company, Zhengzhou 450000, China
[4] China Railway Design Corporation, Tianjin 300308, China; songran@crdc.com
[5] National Engineering Research Center for Digital Construction and Evaluation of Urban Rail Transit, Tianjin 300308, China
* Correspondence: caokelei@ncwu.edu.cn or caokelei456@163.com

Abstract

This study investigates the blast-protective performance of RC slab strengthened on the blast face with various concrete protective layers under contact-detonation loading. The research focuses on analyzing shock wave propagation characteristics, peak pressures at measurement points, energy absorption capacities of the protective layers, the development of damage, and the governing failure mechanisms of the RC slab. The protective layers used for structural reinforcement include Steel Fiber-Reinforced Cellular Concrete (SFR-CC), Asphalt Concrete (AC), Rubberized Concrete (RBC), and Foamed Concrete (FC). Among these, the maximum support rotation angle of the structure strengthened with the SFR-CC concrete layer (T-1) is 0.20°, indicating significantly less damage and deformation compared to other protective schemes. Based on the damage coefficient calculated from the remaining sectional moment of inertia of the protected RC slabs, the destruction grades of the structures at different concrete protective schemes were classified. Among these, the SFR-CC layer exhibits the most effective attenuation of shock wave peak pressure. Additionally, the maximum support rotation angle of the structure strengthened with the SFR-CC concrete layer is 0.20°, indicating significantly less damage and deformation compared to other protective schemes. Damage grades were assigned according to a coefficient derived from the residual sectional moment of inertia of the protected RC slabs. The SFR-CC configuration (T-1) gives the lowest damage index, 0.178, approximately 64.5% below that of the NC scheme, and is classified as slight damage. In contrast to the severe damage sustained by the protected RC slabs strengthened with the NC concrete scheme, those strengthened with the AC, RBC, and FC protective layer schemes exhibit only a moderate damage grade. Empirical formulas predicting the damage index of protected structures under the combined effects of varying blast charges and concrete layer thicknesses were further developed for rapid damage assessment.

Keywords: contact explosion; different concrete protective layers; destructive mode; evaluation of protective effect; damage level evaluation

Academic Editor: Yonghui Wang

Received: 5 June 2026
Revised: 24 June 2026
Accepted: 26 June 2026
Published: 29 June 2026

1. Introduction

Nowadays, the volatile global landscape and the recurrent occurrence of terrorist bombing attacks pose a grave threat to the operational safety of both civilian and military infrastructure. These incidents not only cause substantial economic losses but also directly endanger the safety of people's lives and property [1–4]. As a conventional load-bearing component in building structures, reinforced concrete (RC) slabs play a pivotal role in determining the overall protective capacity of structures, with their blast resistance serving as a key influencing factor [5,6]. Normal concrete exhibits significant brittleness and low tensile strength. Although the addition of reinforcement can improve its tensile properties to some extent, Reinforced Concrete slabs remain susceptible to surface spalling, edge collapse, and extensive structural damage under intense explosive impact loads [7–10]. Therefore, researching technical methods to effectively enhance the blast resistance of RC slabs has become a key focus in protective engineering.

Current research scenarios related to explosions mainly cover three working conditions: contact explosions, near-field explosions, and underwater explosions. Contact explosions are characterized by high peak pressure, short duration, and strong localization of load effects. Near-field explosions feature a broader load action range and more prominent global bending responses of structures. Owing to the high density and high wave impedance of water media, underwater explosions differ substantially from air explosions in terms of shockwave propagation, interface reflection, and bubble pulsation effects. Accordingly, the mechanical mechanisms and protective performance of various concrete protective layer reinforcement schemes proposed in this study are investigated exclusively under an air environment. Scholars worldwide have conducted numerous studies on enhancing the blast resistance and protective mechanisms of reinforced concrete structures subjected to explosive impact loads. These studies can be broadly categorized into two approaches: one focuses on improving the structural blast capacity by optimizing the material's inherent strength characteristics; the other aims to enhance overall blast resistance by applying protective layers to the structural surface, leveraging their superior mechanical properties. Common protective materials include polyurea [11,12], POZD [13–15], and aluminum foam [16–18], all of which exhibit high energy absorption capabilities. For example, Wu et al. [19] found that coating reinforced concrete slabs with polyurea significantly enhances structural blast resistance, and better maintains structural integrity. Huang et al. [20] investigated the destruction characteristics and damage modes of blast-resistant polyurea-coated RC plate at contact detonation, analyzed the dynamic response and energy dissipation effects of various schemes, and examined the macro- and micro-scale damage morphology of polyurea. Their findings demonstrated that polyurea exhibits superior energy dissipation performance under a specific loss factor. Wang et al. [21] analyzed the blast performance of POZD-coated corrugated steel plate composite structures under contact detonation, elucidating the mechanism by which the POZD coating enhances structural blast resistance. Subsequently, focusing on the effects of corrugated steel plates with varying angles on blast resistance, they derived an empirical formula for maximum deflection that incorporates both the corrugated steel plate parameters and the TNT explosive charge mass. Li et al. [22] investigated the factors influencing the blast resistance of aluminum foam cylinders under internal blast loading. By conducting tests with varying relative densities and internal blast loads, they characterized the morphological defects in both the inner and outer layers. The results indicated that, under the condition of a homogeneous aluminum foam layer, the specific energy absorption decreases as the relative density deviates from its optimal level. Additionally, reinforcing the surface layer of structures with concrete materials possessing superior mechanical properties has become a prominent research focus in the field of protection.

Common concrete materials used as protective layers include Steel Fiber-Reinforced Cellular Concrete (SFR-CC) [23], Foamed Concrete (FC) [24–26], Asphalt Concrete (AC) [27,28], and Rubberized Concrete (RBC) [29,30]. For instance, Cao et al. [31] evaluated SFR-CC protective layers under underwater blast loading and found that the protection effect first increases and then decreases with steel-fiber volume fraction, with the 15% fiber-volume mixture performing best. Shang et al. [32] examined FC layers with different thicknesses on strengthened RC walls and concluded that the mitigation effect depends on impedance behavior as well as stress accumulation and release under high-velocity impact, while layer thickness mainly controls FC crushing and stress attenuation. Zhao et al. [33] combined reinforced concrete with functionally graded materials (FGMs) to analyze the impact compression behavior and blast resistance of layered graded rubberized concrete. Their results demonstrated that rubberized concrete with a concave gradient configuration exhibits superior impact resistance compared to conventional homogeneous rubberized concrete, showing significantly enhanced stress wave dissipation capacity and blast resistance under high-velocity explosive impact loading. Wu et al. [34] conducted a numerical simulation study on AC under impact loads, validating the expressions for the strength surface and damage factor within the constitutive model used in the simulation. They proposed a modified damage factor to represent higher failure strain levels, enabling more accurate predictive simulations of AC material mechanical responses. The results indicate that the KCC model can produce simulation outcomes for AC structures that closely align with data obtained from field trials and laboratory tests. In summary, current research in the field of protective engineering primarily focuses on the use of various types of high-performance concrete as structural protective layers. However, significant variations exist in the blast resistance of different high-performance concrete materials, and there is a lack of systematic, comparative evaluations regarding the applicability and protective effectiveness of these concrete layers. Therefore, further studies are needed to assess the blast performance of different high-performance concrete materials. In this study, normal concrete (NC), steel fiber-reinforced cellular concrete (SFR-CC), asphalt concrete (AC), rubber-modified concrete (RBC) and foamed concrete (FC) are selected as research materials. These materials differ distinctly in density, compressive strength, deformability and energy dissipation mechanisms, and can cover typical protective behaviors of concrete-based protective layers, including rigid load bearing, pore collapse, fiber toughening and flexible energy absorption. A unified numerical model is established in this paper to comparatively investigate the protective mechanisms of the aforementioned concrete protective layers, with emphasis placed on evaluating their influences on shock wave propagation, peak pressure, energy absorption capacity and damage evolution.

This study investigates the protective effect of RC slabs strengthened with various concrete protective layers on blast-affected surfaces under contact explosions. A multi-medium coupled numerical model of "concrete protective layer-reinforced concrete slab-air-TNT" under contact explosion is established based on the Arbitrary Lagrangian–Eulerian (ALE) algorithm, and systematic investigations are carried out on the energy absorption characteristics, damage development, and failure mechanisms of RC slabs protected by the different concrete layers on their blast-facing surfaces. Damage grades are defined, and the protective performance of various reinforcement schemes is systematically analyzed. The findings provide a theoretical foundation for the design of blast protection in reinforced concrete structures strengthened on blast-affected surfaces subjected to explosive loads.

2. Establishment and Reliability Verification of Multi-Medium Coupling Model

2.1. Experimental Overview

To verify the validity of the ALE method, numerical simulation analyses were carried out according to the contact explosion test conditions provided in the experimental data of existing reference [35]. In the experiment, the concrete slab measured 1500 mm × 1500 mm × 300 mm, with an attached protective layer 20 mm thick. The test materials were specified as follows: the concrete had a strength grade of C40 (compressive strength of 42.5 MPa), and a three-layer steel mesh was constructed using 8 mm diameter reinforcing bars. The longitudinal and transverse spacing of the bars was set at 240 mm (steel bar grade: HPB235), as detailed in Figure 1. A 1.6 kg TNT charge was placed at the geometric center of the reinforced concrete slab, as depicted in Figure 2.

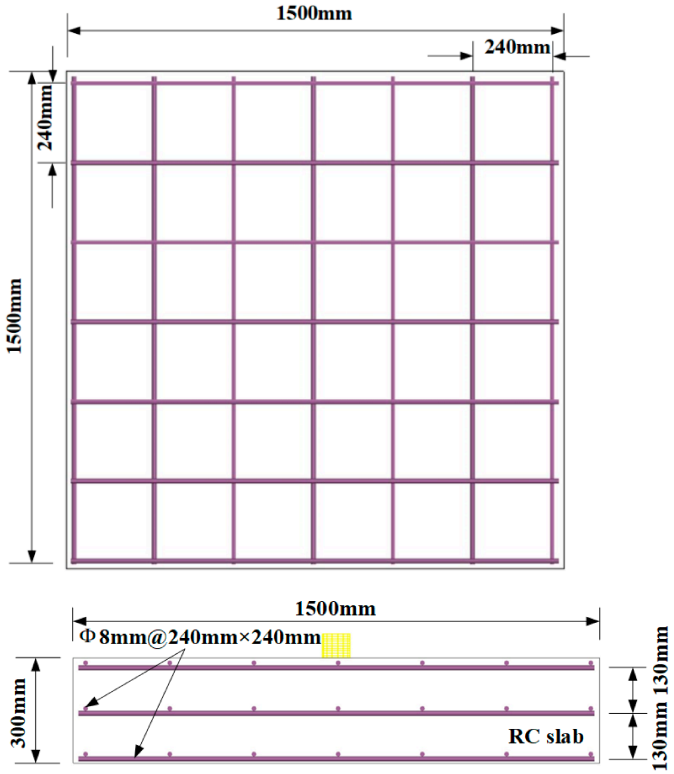

Figure 1. Arrangement of structural dimensions in the test.

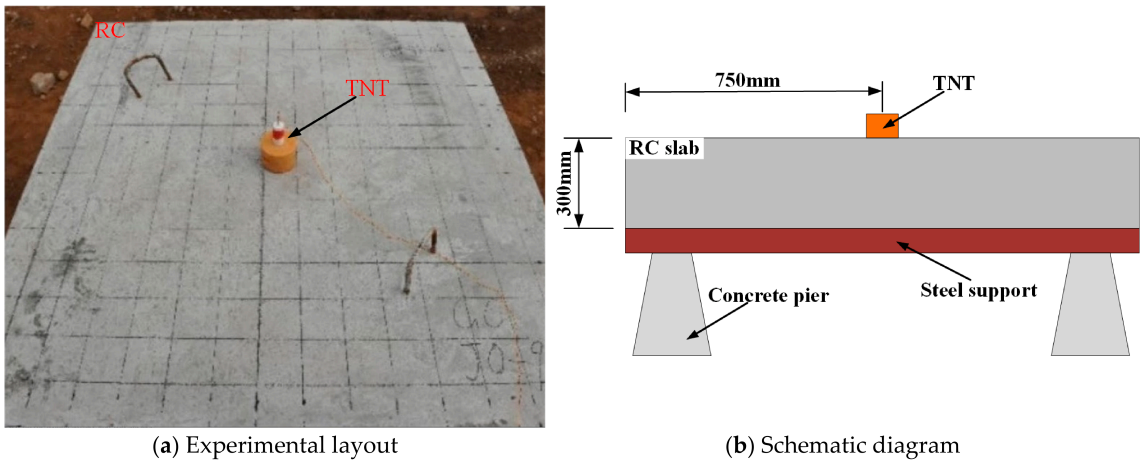

(**a**) Experimental layout (**b**) Schematic diagram

Figure 2. Contact explosion test and structural schematic diagram.

2.2. Construction of Finite Element Model

A three-dimensional simulation model of the "TNT-RC slab-air" coupling system was developed using the ALE numerical method, as illustrated in Figure 3. The model comprises steel reinforcement, concrete, explosive material, and air. The steel reinforcement was represented using BEAM elements, while the other materials were discretized with ALE elements. The element size was set to 10 mm for both the steel reinforcement and concrete slab, and 20 mm for the explosive and air domains. A full-scale model was employed to enhance computational accuracy. Fixed constraints were applied at both ends of the concrete slab, and non-reflecting boundary conditions were assigned to the air domain.

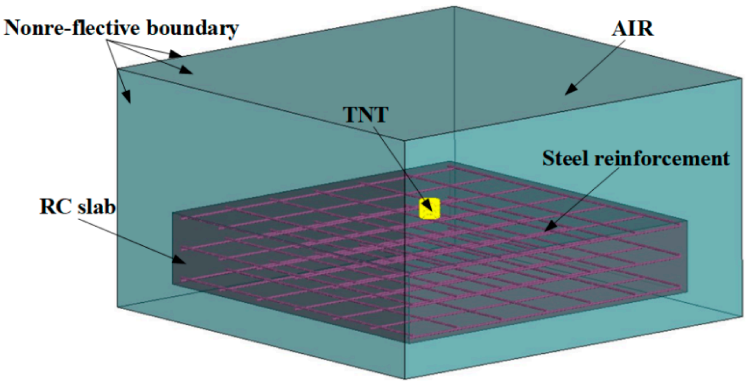

Figure 3. Finite element model.

2.3. Material Parameters

2.3.1. Concrete

The MAT_CONCRETE_DAMAGE_REL3 material model was selected for concrete. This model automatically calculates relevant parameters together with its matched compaction equation EOS_TABULATED_COMPACTION via filling in material mass density, uniaxial compressive strength, strain rate curves and amplification coefficient profiles. Detailed material input parameters are summarized in Table 1, as referenced in Ref. [36].

Table 1. Concrete parameters.

Density/(g/cm^3)	Poisson's Ratio	Tensile Strength/MPa	Compressive Strength/MPa
2.5	0.19	3.7	43.6

2.3.2. Steel Reinforcement

Given that the material model for steel bars must account for the material's mechanical sensitivity to strain rate, the *MAT_PLASTIC_KINEMATIC material model was adopted to characterize HRB400 steel bars. The specific parameters were referenced from [37], as shown in Table 2.

Table 2. Steel.

Density/(g/cm^3)	Poisson's Ratio	Modulus of Elasticity/MPa	Yield Strength/MPa
7.8	0.3	2.07×10^5	400

2.3.3. TNT

To accurately replicate the detonation behavior of TNT, the MAT_HIGH_EXPLOSIVE_-BURN constitutive model was combined with the EOS_JWL state equation to describe the volumetric internal energy variation corresponding to the initial structural volume. The corresponding expression is provided below:

$$p = A(1 - \frac{\omega}{R_1 V})e^{-R_1 V} + B(1 - \frac{\omega}{R_2 V})e^{-R_2 V} + \frac{\omega E_0}{V} \quad (1)$$

In the formula, p is the detonation pressure (MPa); E_0 is the internal energy per unit volume; V_0 is the initial relative volume; A and B are the material pressure coefficients; R_1, R_2, and ω are the dimensionless coefficients of the *EOS_JWL equation of state. The specific material parameters are referenced from Reference [38], with relevant details provided in Table 3.

Table 3. TNT parameters.

Density/(g/cm^3)	A/GPa	B/GPa	R_1	R_2	Poisson's Ratio	V_0	E_0
1.6	373.4	3.74	4.15	0.9	0.35	1	7

2.3.4. AIR

In the numerical simulation, the *MAT_NULL constitutive law was utilized to define air, which was assumed to be a non-viscous ideal gas. *EOS_LINEAR_POLYNOMIAL, formulated as a linear polynomial, was utilized to quantify the functional relation between the initial volumetric internal energy of air and blast shock pressure. The specific relationship is expressed as follows:

$$P_a = C_0 + C_1\mu + C_2\mu^2 + C_3\mu^3 + \left(C_4 + C_5\mu + C_6\mu^2\right)E_0 \quad (2)$$

where P_a stands for the blast pressure of air shock waves, and E represents the internal energy corresponding to unit initial volume. All relevant material parameters can be found in Ref. [39], as presented in Table 4.

Table 4. Air parameters.

Density/(g/cm^3)	Initial Pressure/MPa	γ	E_0/(MJ·kg^{-1})	V_0
1.29	0.101	1.4	2.5×10^5	1

2.4. Validation of the Method

The experimental data reported in existing studies and numerical analyses of the RC slab subjected to contact detonation are shown in Figure 4. In the experiment, a large crater formed on the blast-affected surface of the RC plate, with the steel reinforcement exposed. The crater was 653 mm wide and 595 mm long on the blast-affected surface, while the spallation zone on the back-blast surface measured 720 mm in width and 778 mm in length. The numerical results indicated that the crater on the blast-loaded surface of the RC plate was 610.1 mm wide and 600.1 mm long, whereas the spallation zone on the back-blast surface was 691.7 mm wide and 740.5 mm long. The relative errors between experimental measurements and corresponding numerical simulation dimensions were calculated sequentially. Subsequently, the arithmetic mean of the four groups of relative errors was computed, yielding an overall average error of 3.75%, which falls within the acceptable error range. It can be clearly observed that the experimental and

numerical simulation results exhibit consistent damage characteristics on both the blast-facing and rear surfaces, and the crack propagation on the rear surface of reinforced concrete slabs shows a trend of radial outward diffusion in all cases. This substantiates the practicability together with the computational precision of the numerical simulation approach, accordingly offering a credible simulation foundation for follow-up explorations on the anti-explosion capacity and shielding behavior of RC slabs reinforced with diverse concrete functionally graded protective layers.

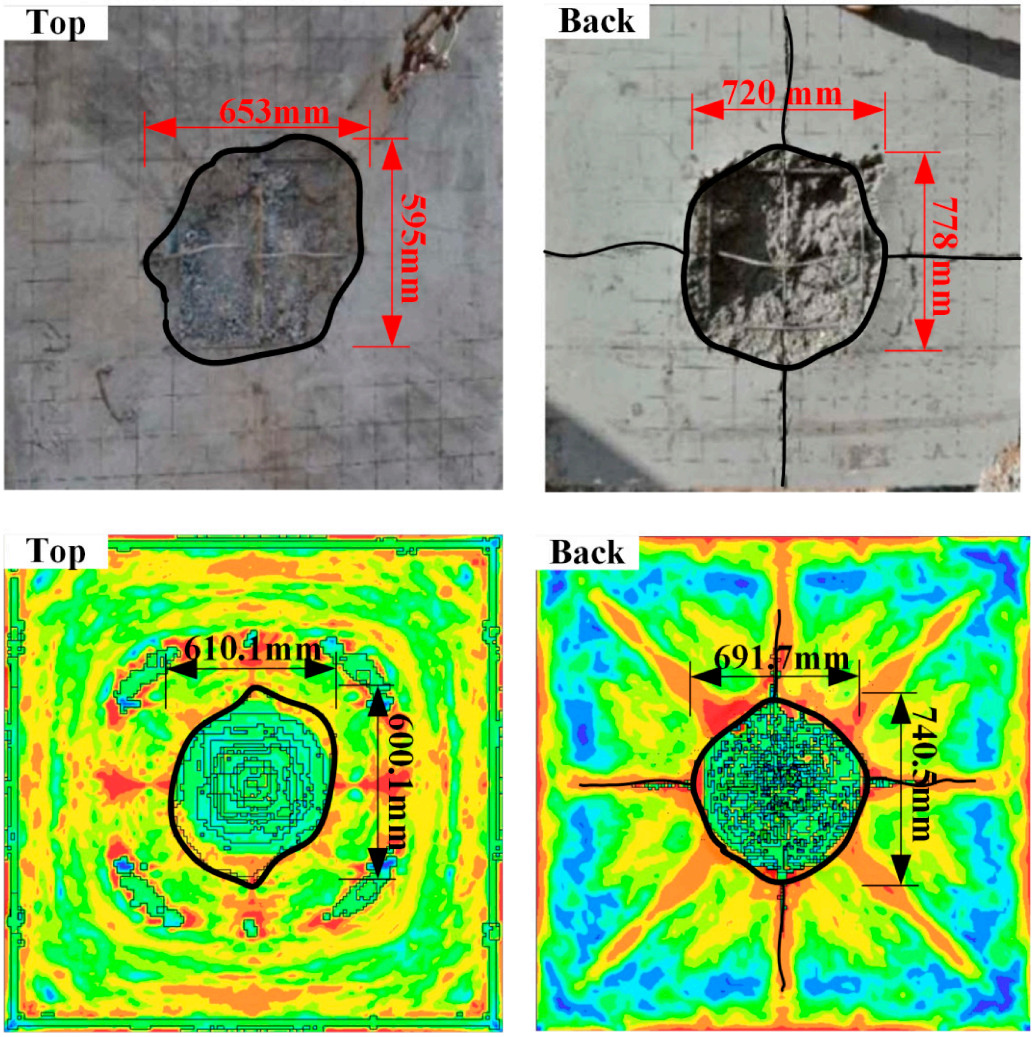

(**a**) Top surface (**b**) Back surface

Figure 4. Comparison of experimental and numerical results.

3. Numerical Simulation of RC Slabs Strengthened with Various Concrete Protective Layers on Blast-Facing Surfaces

3.1. Design of Reinforcement Schemes for Different Concrete Protective Layers

To evaluate the anti-blast behavior of RC plate with different concrete layers on the explosion-exposed surface, this study designed protective structure schemes by varying the types of concrete protective layers. The layers included Steel Fiber-Reinforced Cellular Concrete (SFR-CC), Asphalt Concrete (AC), Rubber Concrete (RBC), and Foam Concrete (FC). Detailed schemes are presented in Table 5.

Table 5. Design of different concrete protective layer schemes.

Grouping	Charge/kg	Protective Layer Position	Concrete Layer	Layer Thickness/mm
T-0	3	blast-facing surface	NC	100
T-1	3	blast-facing surface	SFR-CC	100
T-2	3	blast-facing surface	AC	100
T-3	3	blast-facing surface	RBC	100
T-4	3	blast-facing surface	FC	100

3.2. Protective Layer Material Model and Parameters

3.2.1. Karagozian and Case Model

In this study, SFR-CC [31] (compressive strength: 42.86 MPa), AC [40] (compressive strength: 4.6 MPa), and RBC [41] (compressive strength: 22.8 MPa) were modeled using the K&C model. Due to differences in strength, ductility, and other mechanical properties between these concretes and normal-strength concrete, the strength surface parameters of the material model were revised and improved. The principal parameters corresponding to the modified Karagozian and Case constitutive model are summarized in Table 6.

Table 6. Improved K&C model parameters.

	SFR-CC	AC	RBC
$\rho/(\mathrm{g{\cdot}cm^{-3}})$	2.27	2.3	2.44
f_c/MPa	42.86	4.6	22.5
ν	0.19	0.35	0.2
a_0/GPa	0.012	0.002	0.01
a_1	0.38	0.6	0.584
$a_2/\mathrm{GPa^{-1}}$	3.46	13.5	2.6
b_1	1.6	3.45	1.8
b_2	2.09	0.2	2.1
b_3	1.15	1.15	1.15
a_{0y}/GPa	0.008	0.0018	0.0059
a_{1y}	0.53	2	0.625
$a_{2y}/\mathrm{GPa^{-1}}$	10.49	47.3	16.3
a_{1f}	0.38	0.7	0.792
$a_{2f}/\mathrm{GPa^{-1}}$	5.06	3.7	3.9

3.2.2. Foam Concrete CRUSHABLE_FOAM Model

FC (with a compressive strength of 6 MPa) features lightweight and porous characteristics that enable it to absorb impact energy generated by explosions. Therefore, the MAT_CRUSHABLE_FOAM material model (a crushable foam model) was adopted to represent this material. This model effectively simulates the mechanical behavior of foam concrete through stress–strain curves while accounting for strain rate effects, as illustrated in Figure 5. Detailed parameters are provided in Table 7 [42].

Table 7. FC parameters.

Density/(g/cm^3)	Poisson's	Modulus of Elasticity/MPa	Failure Tensile Stress/MPa
0.4	0.1	342.2	0.2

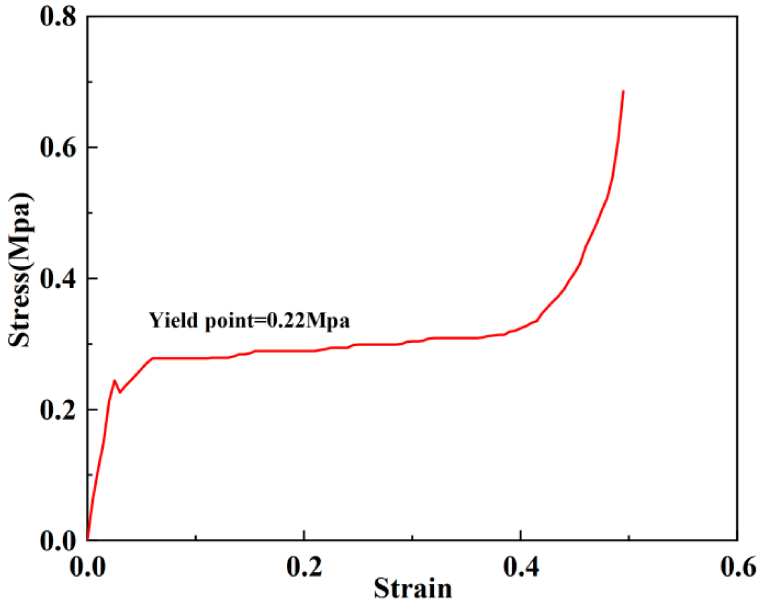

Figure 5. Stress–strain curve of FC.

3.3. Establishment of Numerical Simulation Model

To evaluate the anti-explosion capacity of RC plate structures with various concrete layers on the explosion-impacted surface under blast load, the ALE method was used to develop a multi-medium numerical model of "explosive-air-protective layer-concrete slab", as illustrated in Figure 6. The geometric dimensions of the RC plate in the numerical model were defined as 1500 mm × 1500 mm × 300 mm, with the depth of concrete cover over reinforcing steel bars equals 15 mm. Five layers of steel bar meshes (HRB400 grade) with a diameter of 6 mm were longitudinally arranged at a uniform spacing of 50 mm in both the horizontal and vertical directions. The full-scale model was used for numerical calculation. In the model, the RC slab, protective layer, explosive, air and support were represented by ALE elements, while the steel bars were modeled using BEAM elements. The mesh size of the explosive and air domains was set to 20 mm, and the element size of the other materials was 10 mm, resulting in a total of 1,437,028 elements. A 2 kg TNT was placed at the center of the RC slab. The support component was assigned rigid material properties via the MAT_RIGID constitutive model. The contact interaction between the concrete slab and steel bars was specified via the keyword CONSTRAINED_BEAM_IN_SOLID, while the contact between the protective layer and concrete slab was defined using the keyword CONTACT_AUTOMATIC_SURFACE_TO_SURFACE_TIEBREAK. Both ends of the reinforced concrete slab were assigned fixed constraints. The keyword BOUNDARY_NON_REFLECTING was adopted for the air domain to define non-reflective boundaries, which characterize the infinite propagation of blast waves in air. The material properties of TNT explosive and air adopted in the model were identical to those specified in Section 2.3.

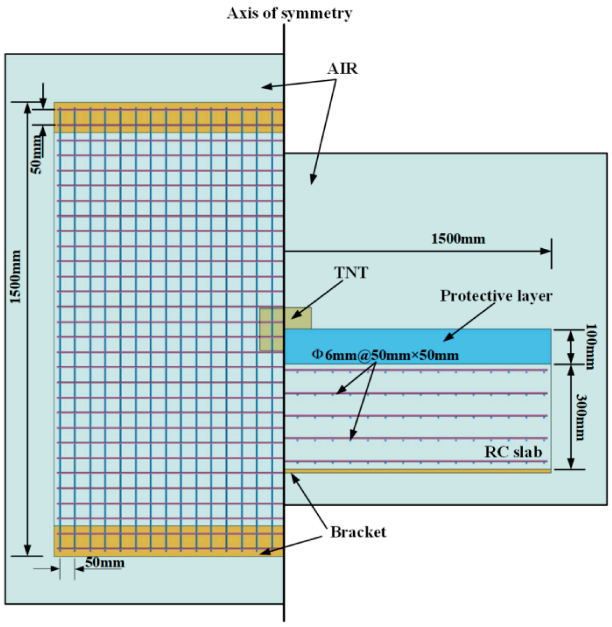

(**a**) Structural dimension layout of numerical model

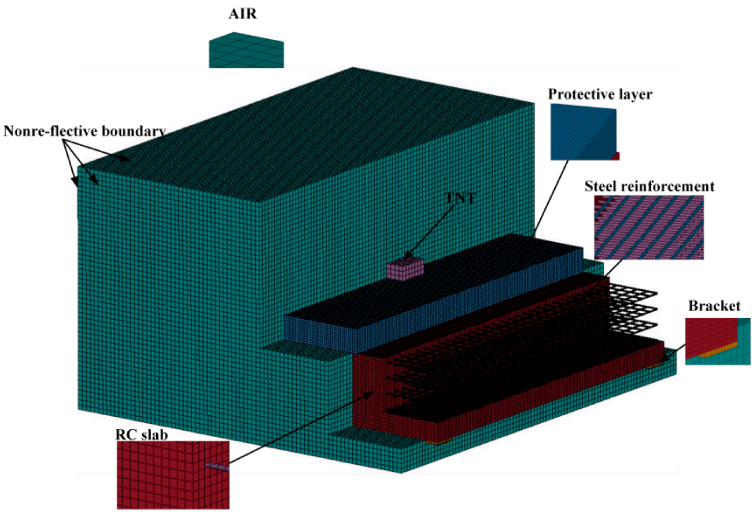

(**b**) Establishment of 3D simulation model

Figure 6. Numerical Model Establishment and Reinforcement Layout.

4. Dynamic Response of RC Slabs with Various Reinforcement Schemes for Concrete Protective Layers

4.1. Propagation Characteristics of Explosion Shock Waves

4.1.1. Features of Shock Wave Propagation in NC Reinforcement Scheme

Figure 7 illustrates the blast wave propagation process for the T-0 configuration with an NC layer. As shown in Figure 7, at 0.05 ms after the blast, the compressive wave generated by the blast directly impacts the NC protective layer, causing rapid compression of the surface concrete and resulting in strain-induced damage to the concrete on the blast-facing side of the concrete layer. At this stage, because the concrete layer and the RC plate have identical wave impedances, the reflection of the blast shock wave at their interface is minimal. Subsequently, the blast shock wave propagates toward the rear face of the RC slab in a spherical wave pattern and penetrates the protected RC plate. At 0.1 ms after the blast, the blast-induced compressive wave reaches the rear face of the slab. Owing to the acoustic impedance discrepancy existing between the concrete at the rear face and the surrounding air, a fraction of the stress wave is reflected at the boundary, generating

a tensile wave, while the remaining portion continues to propagate downward through the RC plate. At this stage, the blast crater in the concrete protective layer expands further, causing surface concrete peeling on the loaded face. By 0.2 ms after detonation, the shock wave reaches the lateral boundaries of the RC plate. Under the continued influence of the tensile wave, spalling failure occurs on the blast-rear surface and side peripheries of the specimen, giving rise to an interior collapse zone inside the RC plate. At 0.35 ms after the explosion, following the shock wave impingement, the explosion-induced crater on the blast-exposed surface of the panel and the scabbing damage region on the blast-back surface expand further. Influenced by boundary effects, the spalling damage along the slab's side edges worsens, accompanied by the initiation of cracks through the thickness. Meanwhile, the collapse zone within the reinforced concrete plate enlarges, and shear failure occurs in the steel reinforcement mesh.

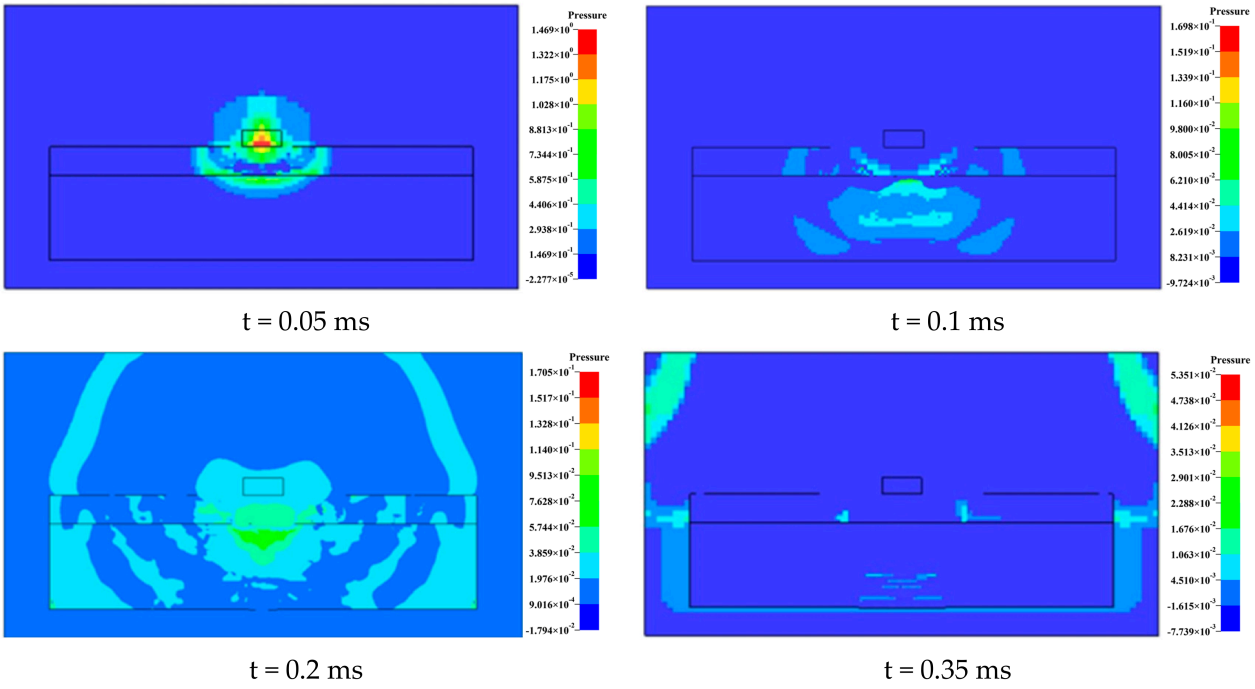

Figure 7. Pressure field distribution of NC scheme.

4.1.2. Characteristics of Shock Wave Propagation in Different Concrete Reinforcement Schemes

To investigate the spread of blast pressure waves through RC plates possessing varying concrete cover layers on the blast-facing side, the current research chose Case T-1 as a typical case to investigate the pressure wave distribution at different time intervals, as shown in Figure 8. Given the similar shock wave propagation characteristics across different protective schemes, Figure 8 clearly demonstrates that direct contact between the explosive and the protective layer causes the blast-induced compressive wave to act on the protective layer immediately upon detonation. At 0.05 ms after the blast, the instantaneous compressive wave induces rapid deformation of the concrete layer and the formation of a blast crater. As the shock wave travels toward the boundary separating the protective layer and the concrete slab, the acoustic resistance mismatch between the two materials causes partial reflection of the pressure wave, generating reflected waves, while the remaining portion continues to propagate toward the blast-rear face as compressive waves. At 0.1 ms after the explosion, the explosion shock wave spreads out in spherical form toward the blast-back face of the RC plate. At this moment, the protective layer is subjected to reflected waves, causing further expansion of the blast crater and the initiation of cracks propagating in both directions. Meanwhile, the concrete on the blast-impacted side of the RC plate

experiences tensile waves, resulting in slight spalling at the interface. Upon the lapse of 0.2 ms after blast initiation, the shock wave reaches the edge of the reinforced concrete plate. Due to the impedance mismatch between concrete and air at the blast-rear face boundary, reflected and transmitted waves are generated at this interface. When the tensile stress wave by rebound tension waves at the back surface of the slab surpasses the superposition of incident compression pulses and the concrete's tensile capacity, spalling damage emerges at the rear side of the structural panel. By 0.35 ms after detonation, the blast shock wave has perforated the concrete slab and continues to propagate outward as transmitted waves. At this stage, damage progressively develops inside the concrete slab and on the blast-back face; additionally, influenced by tensile waves and boundary effects, slight spalling occurs at the edges of the reinforced concrete plate. Compared with the blast wave transmission process in Scheme T-0, the blast wave transmission velocity at characteristic time points of 0.05 ms, 0.1 ms, 0.2 ms, and 0.35 ms decreases following the application of different concrete layers. Therefore, reinforcing the explosion-impacted surface of the RC plate with various concrete layers enhances wave attenuation efficacy, leading to a remarkable elevation in the blast resistance of the structural member.

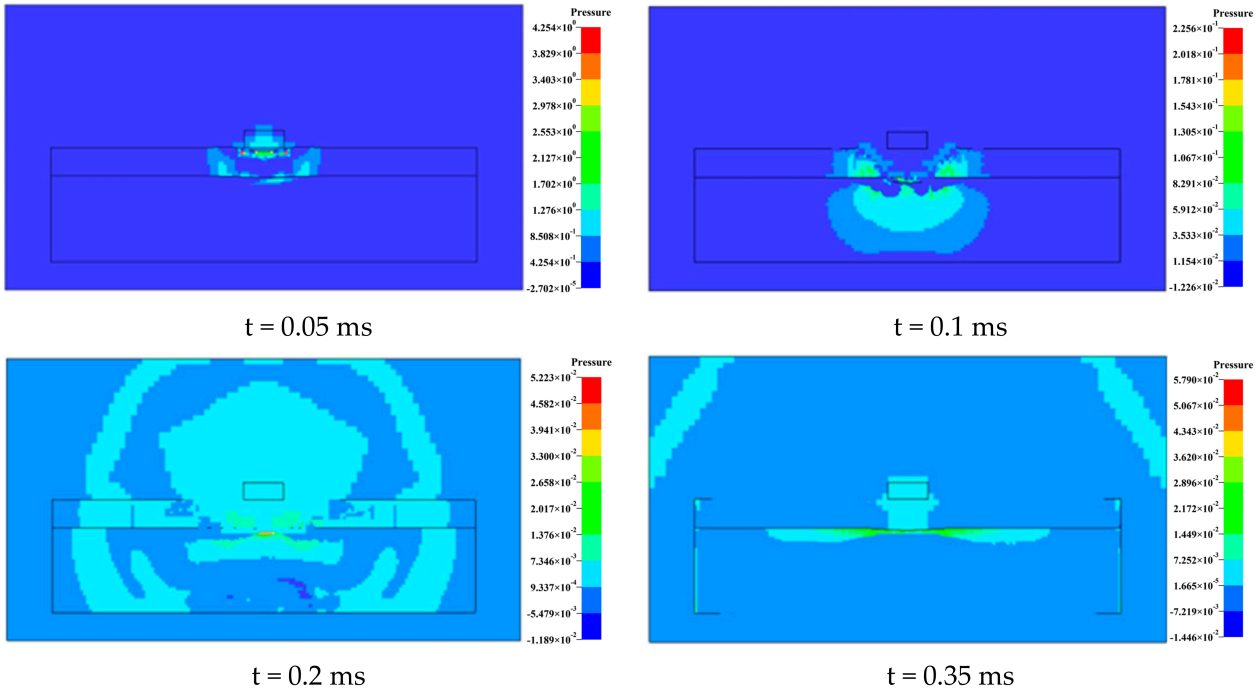

Figure 8. Pressure field distribution of T-1 scheme.

4.2. Peak Pressure at Measuring Points

To investigate the shockwave damping and energy absorption effects of different concrete layers on RC plates strengthened on the explosion-impacted surface under direct detonation impact, four measuring points (Z1, Z2, Z3, and Z4) were arranged at a radial distance of 200 mm from the detonation center. The protective performance of different protective schemes was evaluated by analyzing the pressure-time history curve features of the measuring points and the wave attenuation efficacy of the protective layers under each scheme. Measuring points Z1 and Z2 were positioned at the top and bottom boundaries of the protective covering, respectively, while measuring point Z3 was arranged inside the RC slab at a distance of 150 mm from both Z2 and Z4, as illustrated in Figure 9. Measurement points were arranged on the material elements of both the protective layer and concrete slab. Pressure time–history curves were extracted for individual elements through the post-processing module of the finite element software to obtain pressure values.

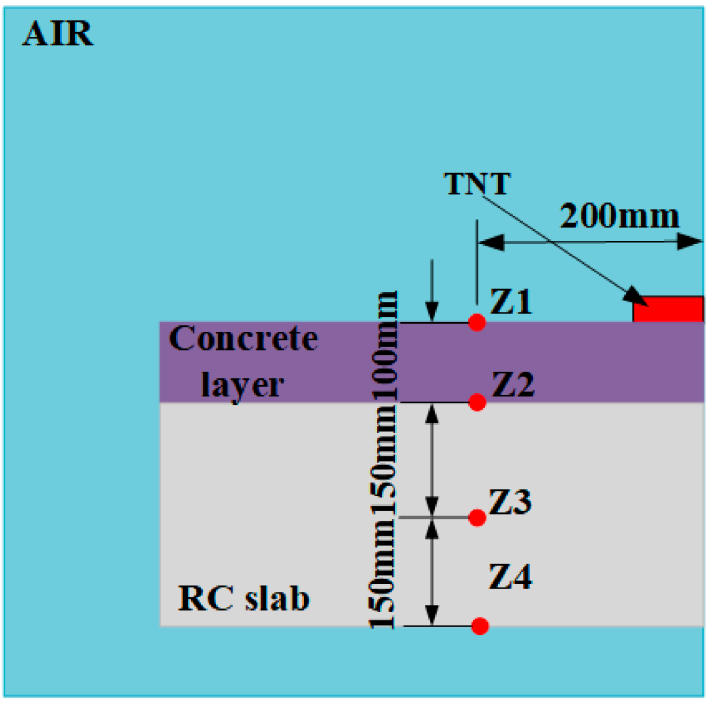

Figure 9. Layout of measuring points.

To clarify the disparities in blast mitigation capacity of RC plates retrofitted with diverse concrete buffer coverings on their explosion-impacted surfaces, the pressure-time history curves at typical measuring points corresponding to the strengthening schemes—namely SFR-CC, AC, RBC and FC) and NC are analyzed and presented in Figure 10. As displayed in Figure 10, the pressure-time history curves for all protective schemes exhibit similar trends, characterized by a rapid pressure rise to a peak value during the initial stage of the blast, followed by a gradual pressure decline and eventual stabilization as the explosion progresses. For the NC overlay strengthening scheme, the pressure-time history curves at representative measuring points reached their peak values at 0.1 ms, 0.15 ms, 0.25 ms, and 0.45 ms, with corresponding peak pressures of 102.5 MPa, 71.5 MPa, 51.3 MPa, and 27.6 MPa, respectively. Under this scenario, the maximum attenuation rate of peak pressure was calculated to be 73.1%. Similarly, an analysis of the pressure-time history curves of slabs retrofitted with various concrete overlay layers revealed maximum attenuation rates of peak pressure of 88.4%, 86.4%, 85.4%, and 79.9%, respectively. Meanwhile, the peak pressures at the representative measuring points exhibited a decreasing trend as the explosion progressed. Compared with the NC overlay strengthening scheme, all the aforementioned concrete overlay configurations achieved higher maximum attenuation rates of peak pressure, revealing that equipping the explosion-exposed surface with assorted concrete overlay layers significantly enhances the attenuation of peak pressure under contact blast loading. As illustrated in Figure 10b, for the slabs retrofitted with the SFR-CC overlay, the peak pressures at the representative measuring points were 53.37 MPa, 21.88 MPa, 12.03 MPa, and 6.15 MPa, respectively. Compared to the NC strengthening scheme, the peak pressures at the corresponding measuring points were reduced by 47.9%, 69.4%, 71.5%, and 77.8%, respectively. It reveals that the SFR-CC overlay enhances the protective performance of the structure through its wave-shaping effect. Similarly, an analysis of the pressure-time history curves for slabs with various concrete overlays retrofitted on the blast-facing side shows that the peak pressures at all measuring points for these protective schemes are lower than those observed with the NC strengthening scheme. This demonstrates that retrofitting different concrete overlays on the explosion-impacted surface can significantly

reduce peak pressures at each measuring point. The underlying mechanism is twofold: first, adding the overlay increases the thickness of the composite structure, thereby prolonging the duration of blast wave action on the protected structure; second, the overlay materials exhibit excellent wave-shaping properties within the composite structure. Under contact blast loading, all concrete strengthening schemes outperform the NC scheme in terms of protective effectiveness. These schemes effectively mitigate the transmission of blast waves within the structure, achieving a wave-dissipating effect. The measured peak pressures at the measuring points of each protective scheme, after retrofitting the blast-facing side with different concrete overlays, are presented in Figure 11. As shown in Figure 11, compared to the NC strengthening scheme, the peak pressures at representative measuring points for all schemes with various concrete overlays are reduced, further demonstrating that retrofitting with different concrete types provides favorable protective performance. To determine the most effective shielding layout for all distinct concrete configurations, the peak pressures at representative measuring points Z1 and Z2 on both sides of the overlay were analyzed. Additionally, the attenuation rate of peak pressure after the blast wave transmitted through the overlay was used as the evaluation criterion for the protective effectiveness of the different schemes. Specifically, for the SFR-CC strengthening scheme, the peak pressures at measuring points Z1 and Z2 were 53.37 MPa and 21.88 MPa, respectively, corresponding to a peak pressure attenuation rate of 59.0%. By analogy, the peak pressure reduction ratios of shockwaves penetrating the overlays of other concrete strengthening schemes (AC, RBC, and FC) were 43.4%, 31.5%, and 44.3%, respectively. In a comprehensive comparison, the peak pressure attenuation performance of the reinforcement scheme using the SFR-CC protective layer surpasses those of other concrete-based reinforcement schemes, effectively enhancing the blast performance of the protected RC plates. This is because the porous structure of SFR-CC endows the material with excellent blast wave dissipation capacity, while the incorporation of steel fibers significantly improves its mechanical strength. Therefore, it is recommended that SFR-CC be employed as the protective solution for the blast-resistant design of RC slab structures with front-blast-side reinforcement under contact explosion scenarios.

4.3. Different Concrete Protective Layers Absorb Total Energy

Under the extreme dynamic loading conditions of contact explosions, the energy absorption performance of the concrete layer is a critical indicator for evaluating its effectiveness in protecting reinforced concrete slabs. Superior energy absorption capacity can remarkably buffer the shockwave and weaken the propagation of energy to the underlying structure, thereby mitigating the extent of damage sustained. To investigate the blast wave mitigation and energy absorption effects of RC plate reinforced with various concrete layers on the explosion-impacted surface, this study evaluates protective schemes with enhanced energy absorption performance by analyzing the energy absorption time–history curves and the steady-state total energy dissipation (the sum of internal energy and kinetic energy) of each buffer coating subjected to explosive impact. The goal is to provide a theoretical foundation for the selection and design of practical protective engineering solutions.

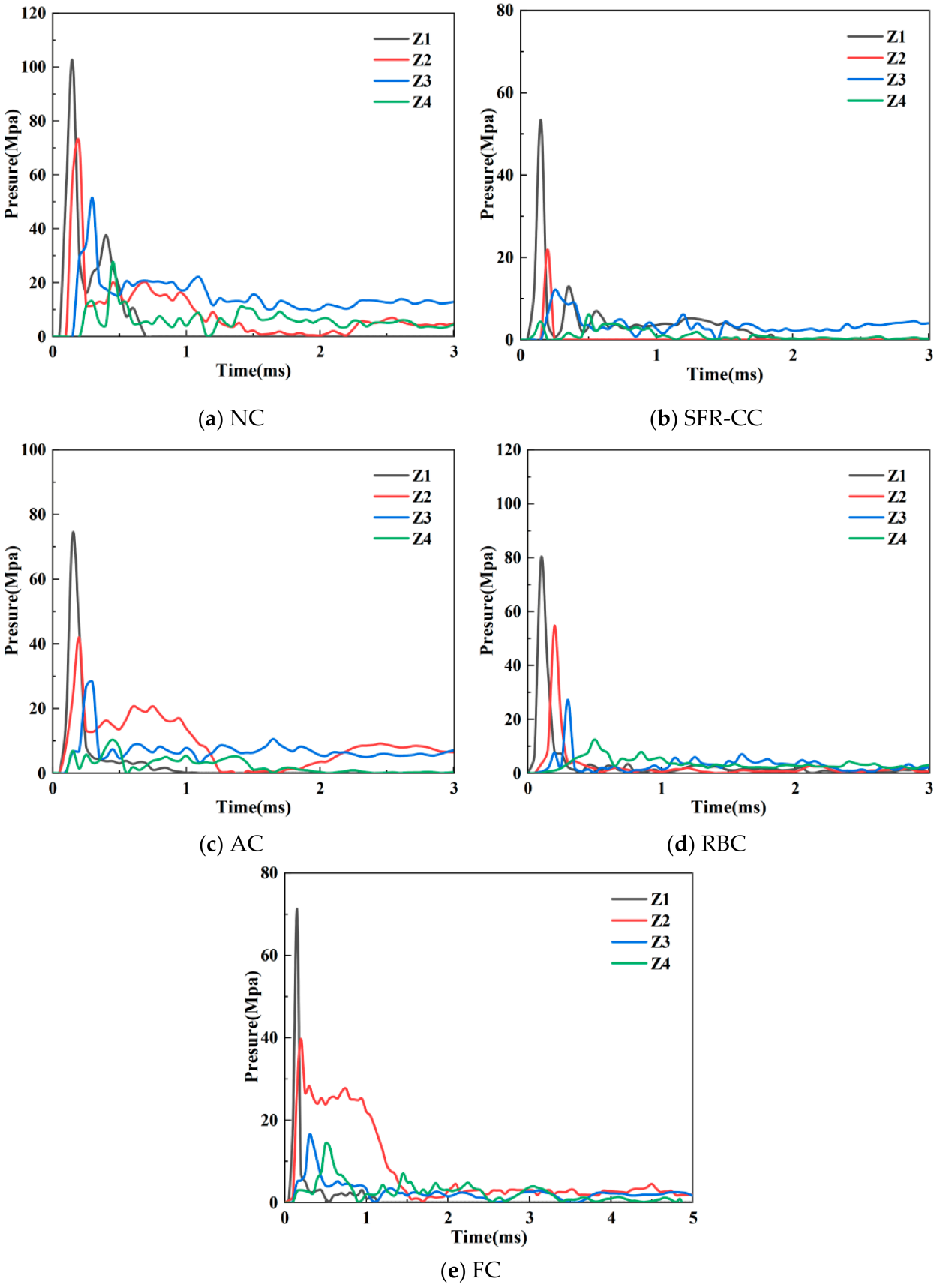

Figure 10. Pressure curves of various reinforcement schemes.

Figure 12a illustrates the energy absorption time–history curves of concrete plates reinforced with various concrete layers on the explosion-impacted surface. The energy

absorption profiles of these concrete layers exhibit similar trends following the application of different materials. During the initial explosion phase (0–0.2 ms), the ultra-high intensity blast shock wave impacts the surface of the protective layer, causing a stepwise increase in energy absorption that rapidly reaches its peak. Subsequently, as shockwaves permeate the inner region of the concrete layer between 0.2 ms and 0.5 ms, the energy absorption decreases due to mechanisms such as structural crack propagation, penetration, and kinetic energy dissipation from fragments. After 0.5 ms, the processes of structural fragmentation and stress wave propagation are essentially complete; the protective layer reaches a quasi-static equilibrium state characterized by the formation of a stable fragmentation zone, and the energy absorption values stabilize. The energy absorption values for the different concrete protective layers (SFR-CC, AC, RBC, and FC) are 5.13 kJ, 3.63 kJ, 4.23 kJ, and 4.05 kJ, respectively. Compared to the NC protective layer (with a total energy absorption of 3.35 kJ), the total energy absorption of the reinforced concrete layers is significantly higher. It reveals that laying an extra concrete covering can effectively absorb the energy of shock pulses, thus cutting down the energy transmitted to the reinforced concrete plate, minimizing damage, and markedly improving the anti-blast capacity. Notably, the scheme reinforced with the SFR-CC layer exhibits a total energy absorption of 5.13 kJ, representing a peak increase of 41.3% compared to other concrete layer schemes, demonstrating superior energy absorption performance. This is mainly attributed to the superior fiber-reinforced toughening performance of SFR-CC material: interconnected or closed pores inside the material dissipate a large amount of energy under impact loading. In summary, among the various concrete protective layers used for front-blast-side reinforcement, the SFR-CC protective scheme delivers the best energy absorption performance, resulting in the protected RC slab bearing the least energy and achieving optimal protection. Therefore, SFR-CC is recommended as the structural design choice for the blast layer in front-blast-side reinforcement of RC panels under close-in detonation conditions.

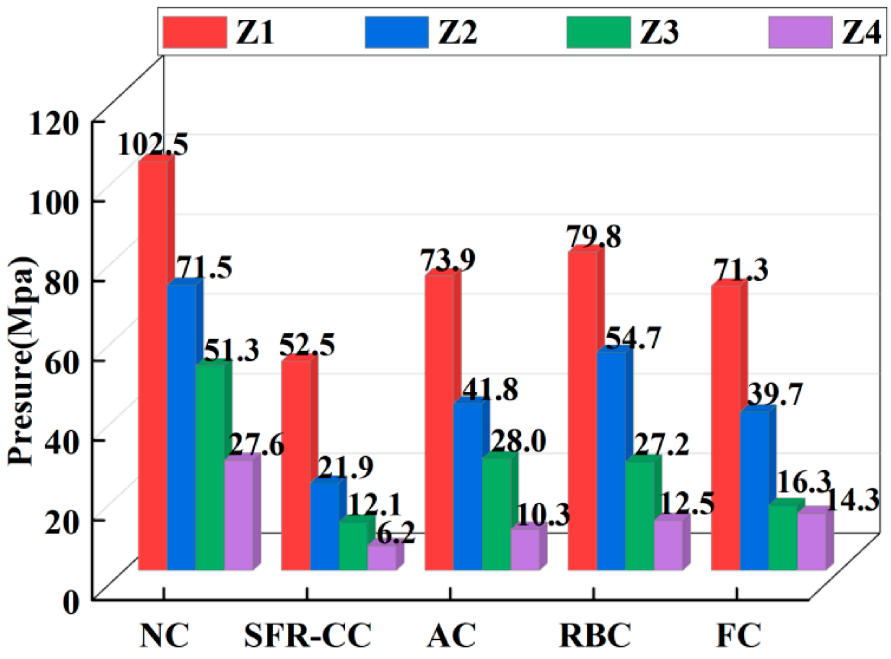

Figure 11. Peak pressure of various reinforcement schemes.

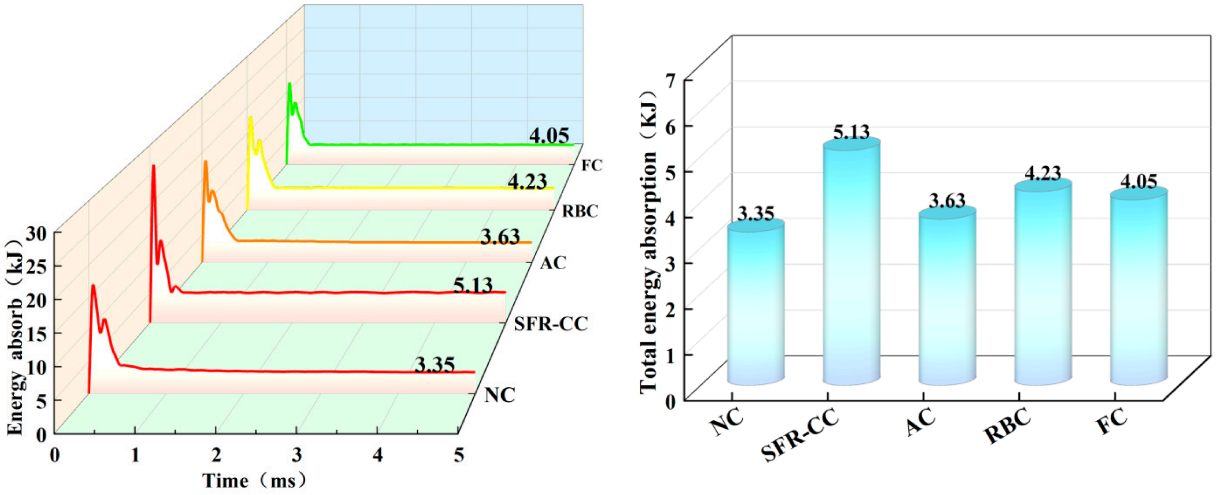

(**a**) Energy absorption time history curve (**b**) The protective layer absorbs total energy

Figure 12. Total energy of different protection schemes.

5. Damage Process and Mode of RC Slab Structure with Various Concrete Layers

5.1. Analysis of Damage Evolution Process

To better elucidate the damage evolution process of protected RC plate subjected to contact explosions under various concrete layer retrofitting configurations, this study analyzed the damage characteristics of the plates at key time points. It systematically revealed the protective effectiveness of different reinforcement schemes and their temporal evolution, as illustrated in Figure 13. Figure 13 clearly shows that the damage evolution processes across the various reinforcement configurations are approximately similar. At the early stage of the blast, the concrete layer is instantly impacted by the blast wave, undergoing rapid compression followed by damage. As the explosion shock wave penetrates the concrete layer and reaches the RC plate, the concrete at the explosion-impacted side experiences compressive stress, resulting in the formation of a crushed zone in certain reinforcement schemes. Subsequently, the blast pressure wave travels to the back-blast surface of the RC slab and reflects, subjecting the rear surface concrete to tensile waves that cause spalling damage. In the later stage of the explosion, internal damage within the protected RC slab gradually expands, forming a collapse zone. Ultimately, the damage stabilizes, with concrete spalling occurring on the front-blast surface and its edges, while the fragmentation region at the rear blast face expands, together with the generation of fractures on the lateral surfaces of the RC slab.

A further investigation into the failure behaviors of the protected RC plates at typical moments following a contact explosion reveals obvious disparities in the severity of destruction among various concrete schemes at these critical time points. At a post-detonation time of 0.05 ms, the structure is in the initial shock compression stage. The blast pressure pulse spreads swiftly within the concrete layer, instantaneously compressing the concrete layer. This subjects the material in the region of the concrete layer adjacent to the explosion center to extreme compressive damage, resulting in the formation of a crushed zone. In the NC reinforcement scheme, a high-intensity compressive damage core zone develops in the protective layer directly beneath the explosion center, exhibiting a relatively severe degree of damage. Due to their lower elastic modulus and higher damping properties, AC and RC can effectively dissipate shock waves, resulting in a larger compressive damage core zone compared to the NC protective scheme, but with a milder degree of damage. When the detonation duration reached 0.2 ms, the shock wave traveled to the non-detonation

surface of the RC plate and was reflected, generating a tensile wave; however, no damage was observed in the surface concrete layer. In the NC protective layer reinforcement scheme, an internal tensile damage zone developed within the concrete slab, indicating the onset of crater formation. In contrast, the FC and SFR-CC protective schemes allowed the protective layers to absorb substantial blast energy, resulting in severe damage to the layers themselves; nevertheless, they significantly attenuated the transmission of blast energy to the internal structure. Additionally, the formation of a fragmented layer played a significant role in blast buffering. At a detonation duration of 0.65 ms, repeated impacts from the reflected tensile wave on the non-detonation surface of the reinforced concrete slab induced spalling of the surface concrete, further aggravating damage to the protective layers. Meanwhile, the bending response of the slab's mid-section began to manifest, and the internal crater zones of the concrete slabs under all reinforcement schemes gradually expanded. The damage was primarily characterized by the integral failure of the protective layers and progressive damage propagation within the reinforced concrete slabs. For the SFR-CC protective scheme, the fiber reinforcement effect was fully realized at this stage: the fibers effectively bridged microcracks, preventing their coalescence into macroscopic cracks, thus markedly elevating the material's tensile resistance and post-cracking ductility of the material. Consequently, the crater's radial span and penetration depth of the zone were substantially smaller than those observed in the NC reinforcement scheme, and the crack network inside the slab was noticeably sparser, with limited propagation in crack width and length. When the detonation duration reached 3.0 ms, the crater zone and spalling area on the non-detonation surface of the reinforced concrete plate further expanded, resulting in pronounced delamination phenomena. At this moment, the blast impact process was essentially complete; the stress wave energy had either dissipated or transmitted beyond the structural boundaries, and the structural damage morphology had stabilized. In the RC slab reinforced with the NC layer scheme, a severe network of penetrating radial and circumferential cracks developed in the midsection, resulting in significant deflection deformation. As presented in Figure 13b, the reinforced concrete plate protected by the SFR-CC protective layer reinforcement scheme exhibited minimal damage: at a detonation duration of 0.05 ms, no damage occurred in the RC plate, while the concrete layer rapidly failed under the compressive wave and gradually formed a blast crater with a significantly smaller extent than that observed in the NC protective layer. At a post-detonation time of 0.2 ms, the explosion wave reaches the back-blast surface and reflects, generating a tensile wave. At this stage, neither spalling damage nor collapse zones are observed on both the impact-facing and rear faces of the RC plate. When the blast time reaches 0.65 ms, spalling damage occurs on the rear face of the RC plate resulting from reflected tensile waves. Simultaneously, a collapse zone gradually develops within the concrete slab, accompanied by crack initiation. By 3.0 ms, the collapse zone within the concrete slab reaches its maximum extent, with localized damage concentrated near the explosion center. The structural damage mode stabilizes while maintaining good overall integrity. Compared to the NC protective layer scheme, the degree of damage at key time points is significantly reduced. For structural engineering practice, SFR-CC is prioritized, adopting SFR-CC as the blast layer in the structural design to strengthen the explosion-impacted face of reinforced concrete slabs against contact explosions.

5.2. Analysis of Damage Mechanism

To evaluate the anti-blast capacity of RC slabs retrofitted by diverse claddings on their explosion-impacted faces, a study was carried out to analyze the damage mechanisms of RC plate under various protection configurations, as presented in Figure 14. As displayed in Figure 14, under contact blast loads, the damage evolution mechanism of RC slabs with

different concrete overlay strengthening schemes can be analyzed from three perspectives: blast pressure wave transmission laws, energy dissipation capacity of the concrete layer and the RC plate, and structural damage features.

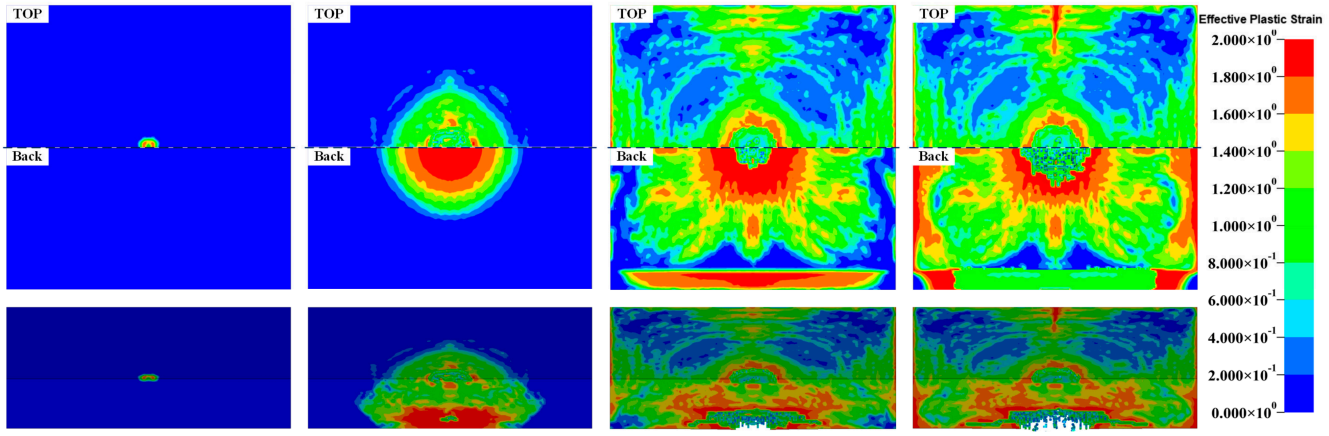

(**a**) NC protective layer reinforcement scheme

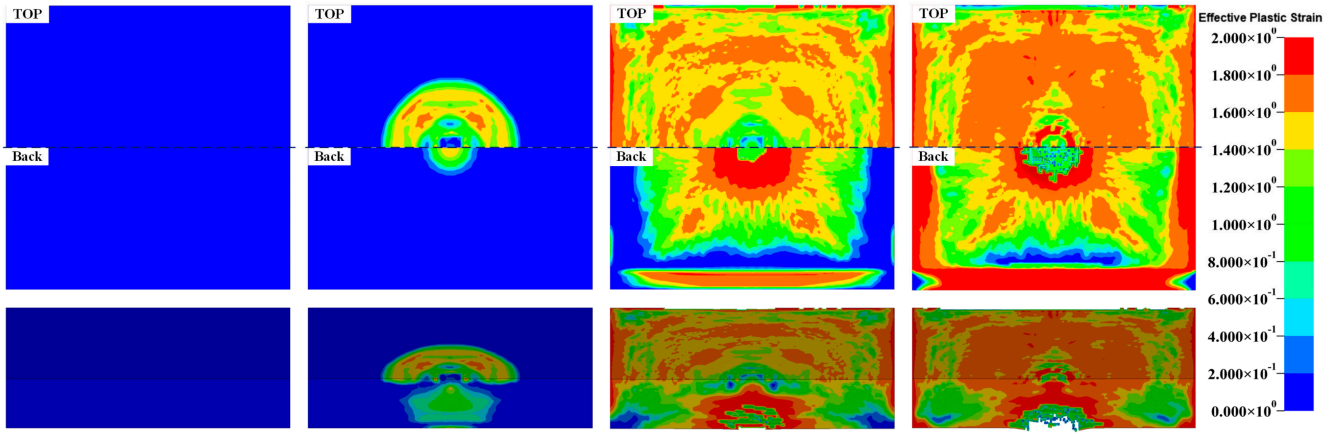

(**b**) SFR-CC protective layer reinforcement scheme

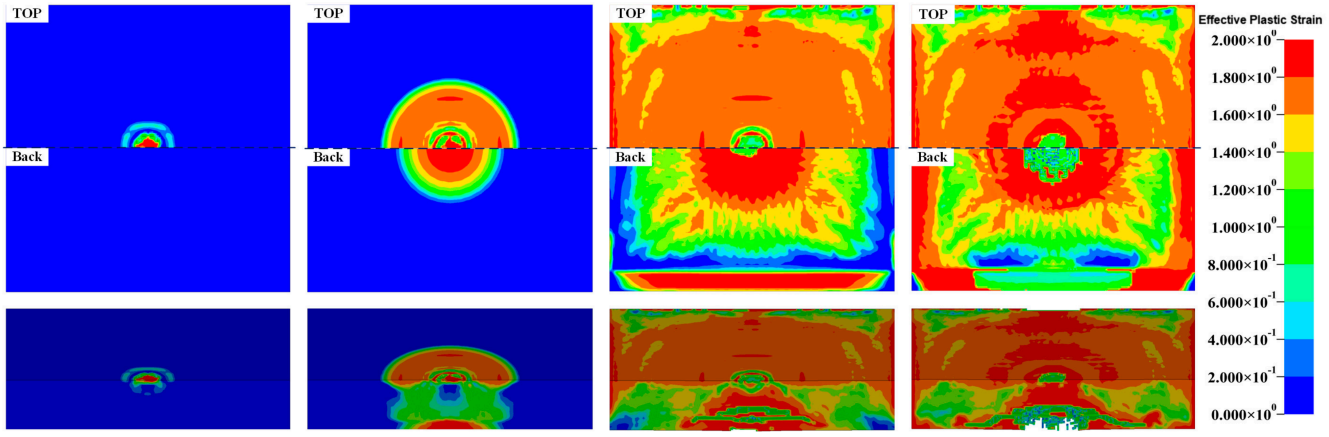

(**c**) AC protective layer reinforcement scheme

Figure 13. *Cont.*

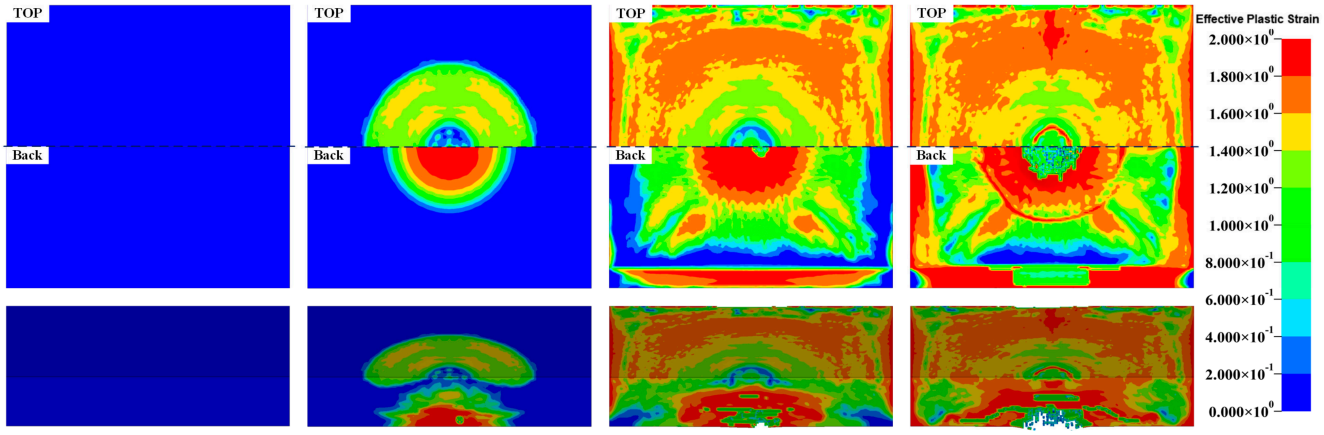

(**d**) RBC protective layer reinforcement scheme

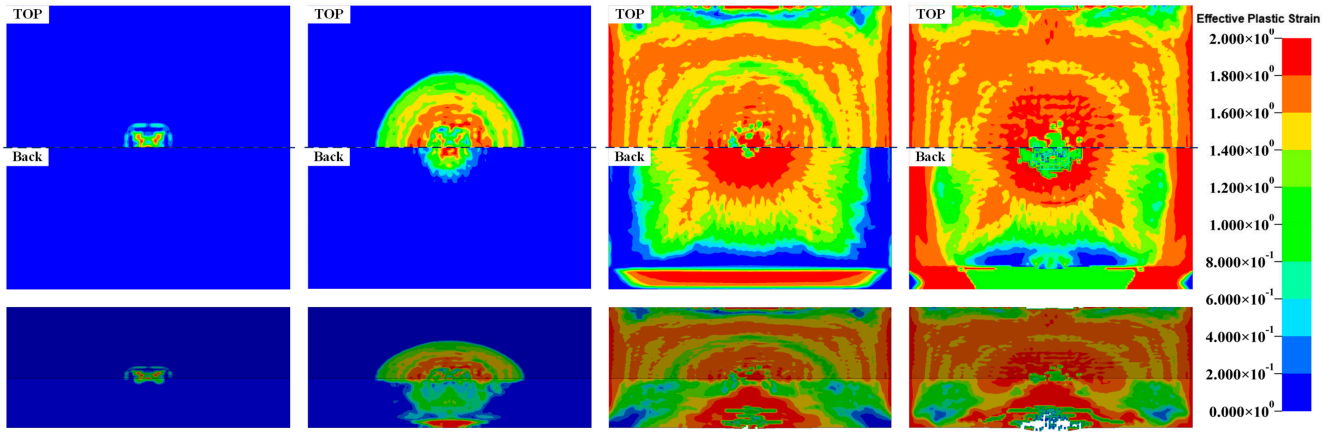

(**e**) FC protective layer reinforcement scheme

Figure 13. Damage evolution process of different concrete protective layer reinforcement schemes.

Regarding blast wave propagation characteristics, the extremely high-temperature and high-pressure detonation products produced upon blast initiation first strike the upper surface of the concrete layer, forming an initial incoming blast wave. Due to the excellent wave attenuation properties of various concrete protective layers, they effectively reduce the intensity of the incident shock wave. Once the pressure wave arrives at the boundary separating the concrete layer and the RC plate, the large acoustic impedance of the concrete induces obvious impedance discrepancy while stress waves transfer from the high-acoustic-impedance material (protective overlay) to the low-acoustic-impedance material (RC plate). Consequently, part of the blast wave is converted into a reflected tensile wave that propagates back into the protective layer, while the remainder transmits into the reinforced concrete slab as a transmitted wave. As the pressure wave continues through the reinforced concrete slab and reaches the back-blast surface interface, the significant impedance difference between air and concrete again generates reflected tensile waves and transmitted waves. From the perspective of energy absorption and dissipation of the protective layer, the total input energy acting on the structure induced by contact explosion is defined as E_{T1}. Under the action of blast loads, the protective layer undergoes a series of damage processes including crushing, cracking, plastic deformation and spalling, which are accompanied by significant energy absorption and dissipation. Specifically, the energy captured by the concrete layer is defined as E_P, and the energy dissipated during wave transmission is E_1. The total energy transmitted into the RC slab after the mitigation effect of the protective layer is E_{T2}. As the blast stress wave transmits across the RC slab, the

material properties of concrete coupled with the synergistic response of reinforcing bars further contribute to energy absorption and dissipation, where the energy captured by the RC plate is recorded as E_R and the energy dissipated during transmission is E_2. Eventually, the residual energy after passing through both the concrete layer and the RC plate is E_3. From the perspective of structural damage characteristics, under contact explosion loads, intense shock waves impinge upon the top face of the concrete layer within an extremely short time, causing severe deformation and fracture of the superficial matrix, thereby generating a crushed region. As the blast wave propagates, damage to the concrete layer continues to expand, gradually forming a blast crater. At this stage, the back-blast surface of the reinforced concrete plate undergoes spalling due to the repeated action of reflected tensile waves, which further develops into a collapse zone. Eventually, the destruction pattern of the RC plate stabilizes, characterized by the continued expansion of the collapse zone and the progressive extension of damage on the front-blast surface and edge regions.

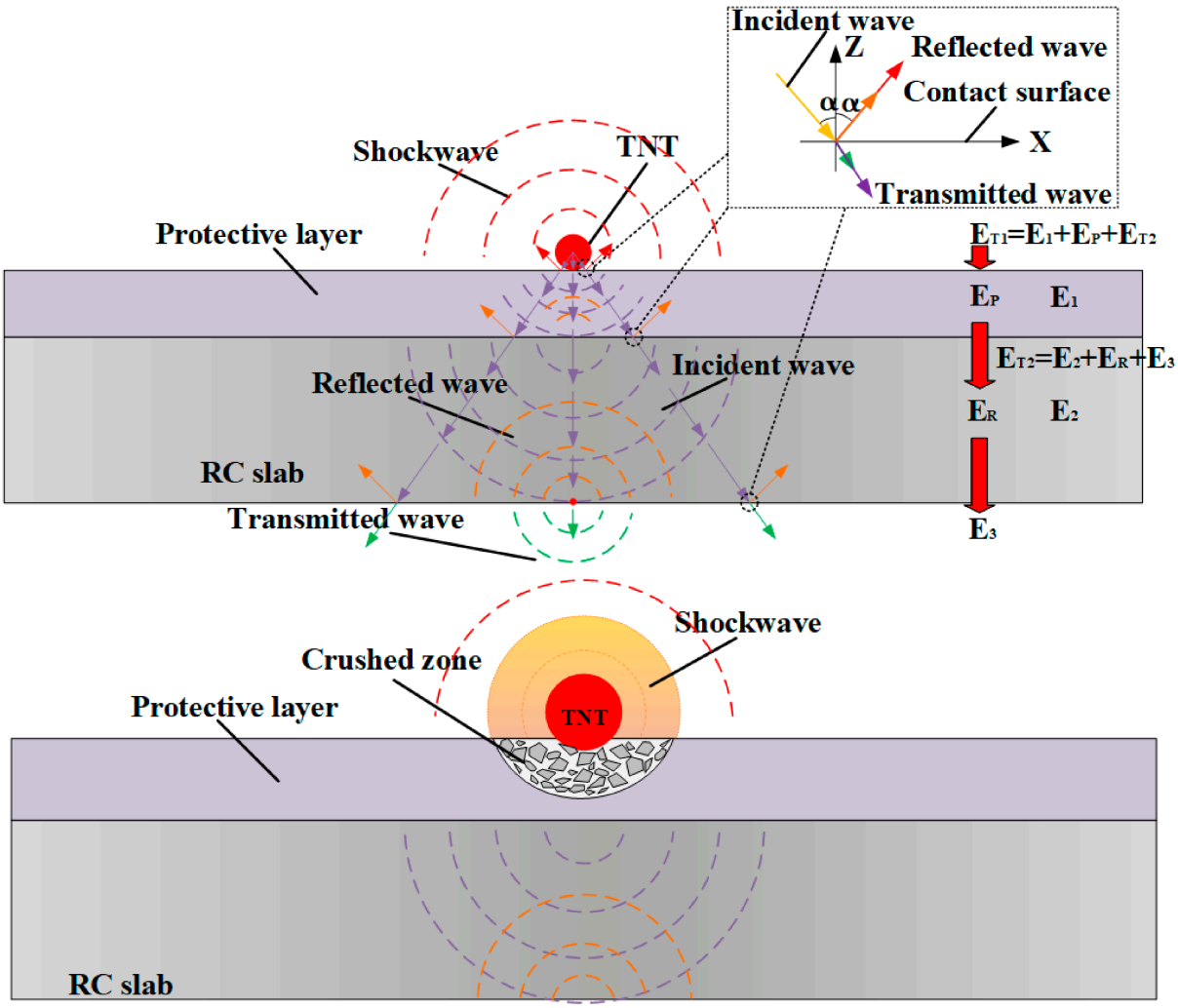

Figure 14. *Cont.*

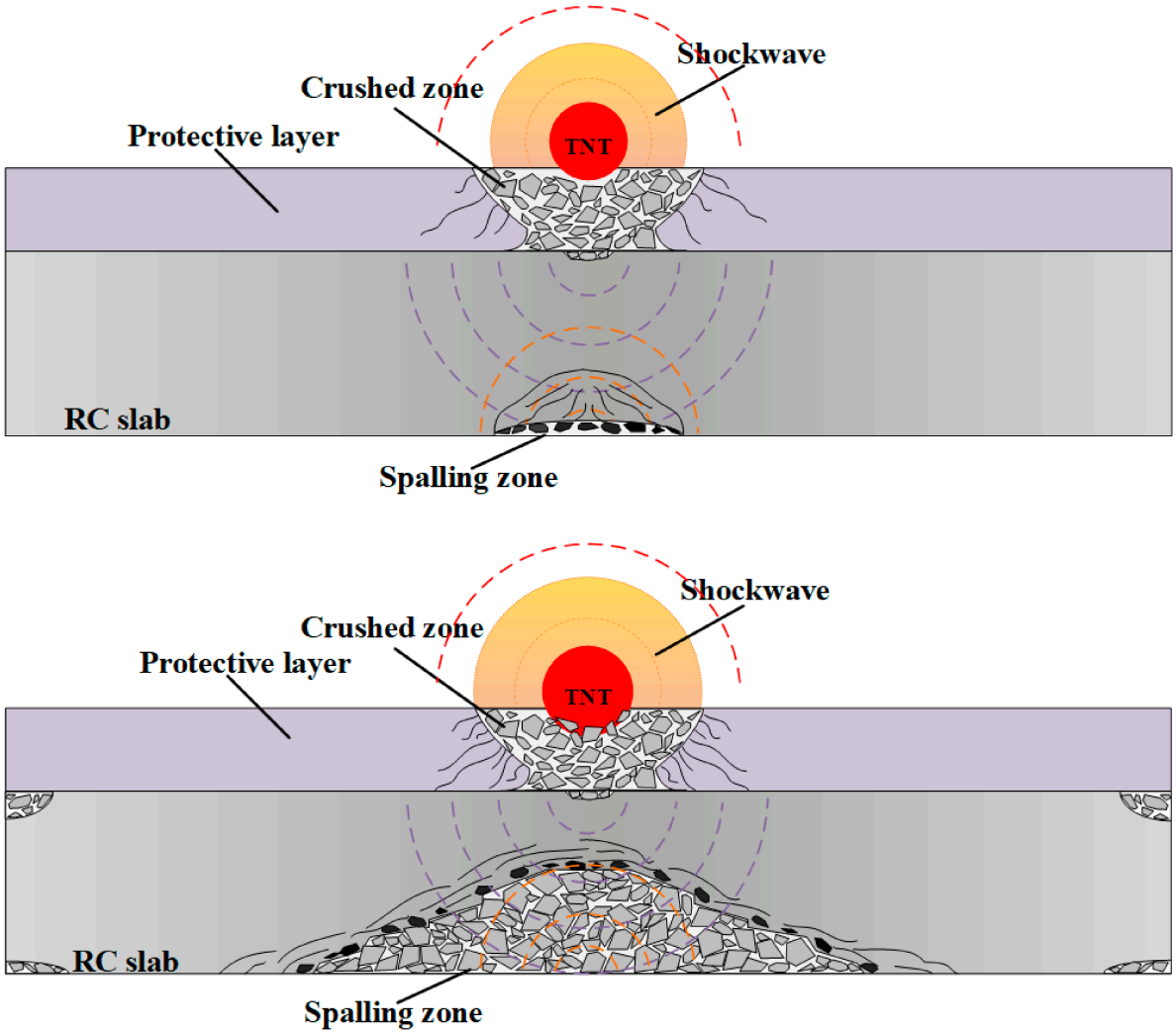

Figure 14. Damage evolution mechanism of different protection schemes.

6. Evaluation of Blast Performance for Structures with Diverse Concrete Layer Reinforcement Schemes

6.1. Maximum Support Rotation

To assess the effect of different protective layer configurations on the failure evolution of RC plates under contact blast loading, this study used the maximum support rotation θ_{max} as the criterion for evaluating failure and failure mitigation in RC plate members subjected to contact blast loads [43]. The maximum support rotation can be calculated from the maximum midspan deflection and half-span length of the RC slab member, as illustrated in the structural schematic diagram shown in Figure 15. Consequently, the blast resistance effectiveness of diverse concrete overlay retrofitting configurations on the protected RC slabs was analyzed according to the magnitude of the maximum support rotation, as expressed in the formula below:

$$\theta_{max} = \arctan\left(\frac{2x_m}{L}\right) \quad (3)$$

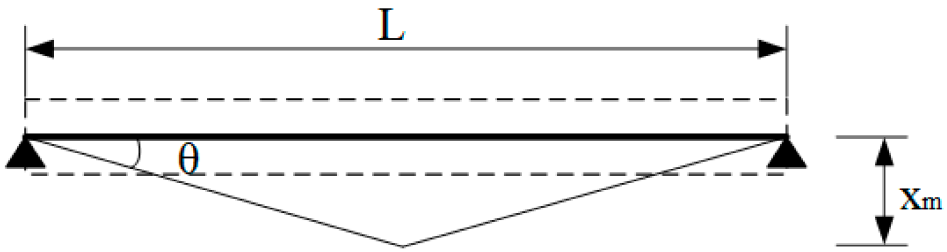

Figure 15. Schematic diagram of support angle.

In the formula: θ_{max} is the maximum support angle; X_m is the mid span deflection of RC slabs under various schemes; L is the net span of the RC plate.

Figure 16 illustrates the mid-span displacement time–history curves and maximum support rotations of reinforced concrete slabs subjected to various protection schemes, featuring reinforced blast-facing surfaces with various concrete players. As displayed in Figure 16a, the mid-span displacement time–history profiles of the RC plate with various concrete layer reinforcement schemes follow similar patterns: initially, no displacement occurs prior to the arrival of the blast stress wave at the slab midspan. Subsequently, the midspan deflection surges to a peak magnitude within a brief duration. Finally, under the action of the reflected tensile wave, the displacement first decreases slowly, then gradually increases until it stabilizes. Among these configurations, the RC plate equipped with the NC concrete overlay yields a peak mid-span displacement of 8.31 mm and a maximum support rotation of 0.65°. The peak mid-span displacements of reinforced concrete slabs protected by different concrete layers (SFR-CC, AC, RBC and FC) are 2.57 mm, 6.10 mm, 3.17 mm, and 2.90 mm, respectively. These values are significantly lower than those of the slab with the NC layer, indicating that reinforcing blast-facing surfaces with various concrete layers can substantially reduce mid-span displacement and, consequently, mitigate damage to the protected RC plate. Figure 16b shows that the maximum support rotations of the protected RC slabs strengthened on the blast-facing surface with various concrete layers are 0.20°, 0.47°, 0.25°, and 0.25°, respectively. All these values are remarkably smaller than those associated with the scheme reinforced with the NC protective layer, with the maximum reduction reaching 71.6%. Among these schemes, the RC plate strengthened with the SFR-CC concrete layer shows the smallest maximum support rotation, at 0.20°, which corresponds to a maximum reduction of 57.5% relative to the other concrete protective layers. The foregoing results suggest that the SFR-CC protective layer provides a markedly enhanced protective effect compared to the other reinforcement schemes. Such performance promotion stems from the synergistic effect of elevated tensile strength and ductility imparted by steel fibers, together with the greater energy-dissipation capacity of the cellular structure for absorbing shock-wave energy. This synergistic effect enables the SFR-CC protective layer to not only effectively dissipate blast-induced energy but also maintain the structural integrity of RC slabs. In view of the above comparative results, SFR-CC overlay is selected as the anti-shock retrofitting solution applied to the blast-facing surfaces of RC slabs subjected to contact detonation loading.

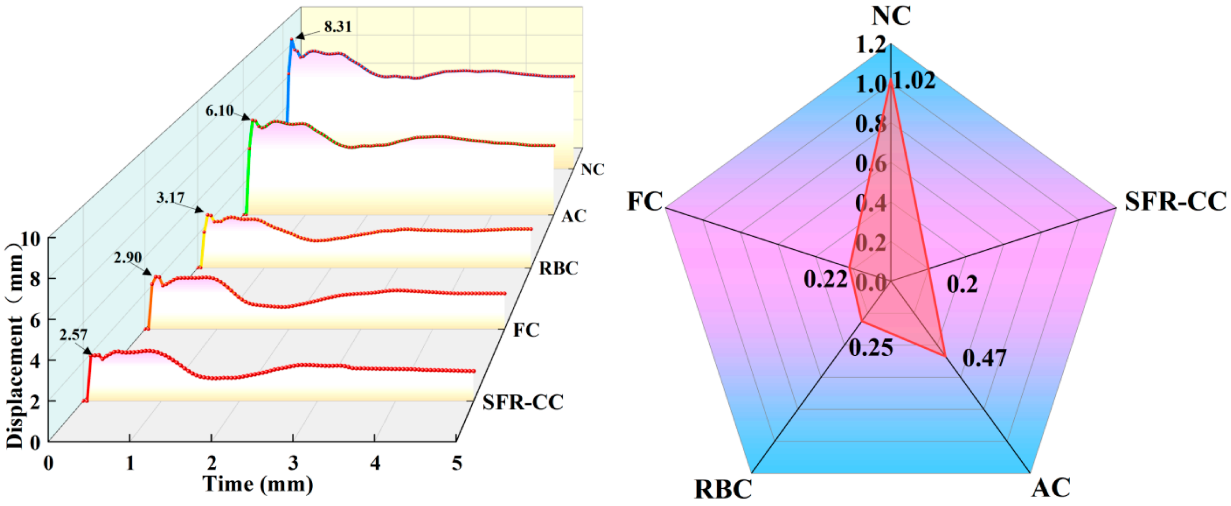

(**a**) Mid span displacement time–history curve (**b**) Maximum Support Rotation

Figure 16. Displacement time–history curves and maximum support angle for different schemes.

6.2. Classification and Prediction of Damage Levels

6.2.1. Classification of Damage Levels

To further analyze the effect of diverse concrete cladding retrofitting on explosion-impacted faces upon the damage severity of shielded RC plate, a classification of the damage levels of RC plate reinforced with various concrete layers was conducted. In this study, the residual sectional moment of inertia of protected RC plate subjected to contact explosion loading is selected as the criterion for evaluating the damage degree of protected structures. Based on damage geometric data and element erosion results obtained from numerical post-processing, a damage index D is proposed via quantitative analysis as a quantitative indicator for classifying the damage grades of RC plate strengthened with various concrete layers on the blast-facing surface [44].

$$D = 1 - I_T / I \tag{4}$$

In the above relation: I_T represents the remaining sectional inertia of the shielded RC slab after blast loading; I denotes the initial sectional inertia of the undamaged slab.

Based on existing research on structural damage assessment under blast loads, the damage levels of reinforced concrete plate can be systematically classified into four grades according to the damage index of slabs with various concrete layer schemes: slight damage, moderate damage, severe damage, and complete damage. The categorized damage levels and their corresponding characteristics are detailed in Table 8.

Given that the irregular cross-sectional dimensions of damaged, blast-loaded reinforced concrete slabs cannot be accurately measured, a simplified computational approach was adopted for the damaged cross-sections of these slabs. To facilitate a unified comparison among various protection schemes, an approximate evaluation index derived from numerical damage morphology is adopted instead of universal damage criteria fully validated by residual bearing capacity tests. For the crater region at the explosion-impacted face and the failure domain on the blast-back side, the regions defined by the measured width and depth were modeled as rectangular zones of complete damage, and their dimensions were incorporated into the calculation of the residual effective cross-section. For other regions, a conservative approach was applied: steel bars were considered to contribute to the effective cross-sectional area only if they remained intact, while fractured steel bars were excluded from the effective area calculation. The formulas for calculating the residual

moment of inertia of the concrete slab cross-section and the steel bar cross-section are provided below:

$$I_{concrete} = \sum \left(\frac{b_i h_i^3}{12} + A_i y_i^2 \right) \quad (5)$$

In the formula: b_i, h_i correspond to the width and depth of undamaged concrete subdomains; A_i stands for the cross-sectional area of each separated concrete segment; y_i represents the offset between the centroid of each segment and the global neutral axis of the slab.

$$I_{steel} = \sum A_{s,j} \cdot d_j^2 \quad (6)$$

In the formula above, $A_{s,j}$ denotes the sectional area of one individual reinforcing bar; d_j signifies the vertical offset between the reinforcement and the section neutral axis.

$$I_{total} = I_{concrete} + I_{steel} \quad (7)$$

Table 8. Disturbance degree.

Damage Index	Disturbance Degree	Destructive Features
[0, 0.2)	Slight damage	Local damage develops in the structure, accompanied by fine surface cracks. The steel bars do not yield, and the structure maintains good performance.
[0.2, 0.5)	Moderate damage	Large-area surface damage occurs, accompanied by reticulated or diagonal cracks, some of which extend through the slab thickness. The steel bars in the tensile zone begin to yield.
[0.5, 0.8)	Severe damage	Severe deterioration occurs within the concrete matrix; several compressive steel reinforcements rupture, accompanied by through-thickness primary fractures and dense intersecting crack networks.
[0.8, 1.0)	Destruction	The central concrete core undergoes thorough failure accompanied by drastically widened fissures. The slab fragments into discrete segments or suffers total collapse, resulting in full loss of structural bearing capacity.

Figure 17 presents the residual cross-sectional moments of inertia, damage coefficients, and damage level classifications of the protected RC plate corresponding to various reinforcement configurations, for explosion-impacted faces strengthened by various concrete layers. It can be observed from Figure 17 that the residual cross-sectional moment of inertia of the RC plate reinforced with the NC protective layer is significantly lower than those of slabs reinforced with alternative concrete layers. The NC-reinforced slab has a damage coefficient of 0.501, which is classified as severe damage. The damage index of slabs with blast-facing surfaces reinforced by various concrete layers (SFR-CC, AC, RBC and FC) are 0.178, 0.412, 0.397, and 0.302, respectively. These values represent reductions of 64.5%, 17.8%, 20.8%, and 39.7%, respectively, compared to the NC protective layer reinforcement scheme. Based on the damage level classification criteria, the SFR-CC protective layer reinforcement scheme results in slight damage, whereas the other reinforcement schemes lead to moderate damage. The results clearly demonstrate that the damage coefficients of RC plates with blast-facing surfaces reinforced by various concrete layers are all smaller in magnitude compared to the values of the NC layer reinforcement scheme, corresponding to a reduction in damage levels. This indicates that reinforcing blast-facing surfaces with various concrete layers can remarkably mitigate the extent of damage to the reinforced concrete plates. Among these schemes, the SFR-CC layer reinforcement achieves the most significant

reduction in the damage coefficient, with a maximum reduction rate of 61.1% compared to other concrete protective layer reinforcement methods. These results demonstrate that the SFR-CC layer provides a substantially protective effect on reinforced concrete slabs when applied to blast-facing surfaces. This effectiveness is attributed to SFR-CC's dual characteristics of cellular energy absorption and fiber reinforcement, which significantly mitigate the damage sustained by RC slabs. In light of the above analytical outcomes, the SFR-CC overlay is proposed as the explosion-mitigating retrofitting measure on the blast-facing surfaces of RC plate subjected to contact detonation loading.

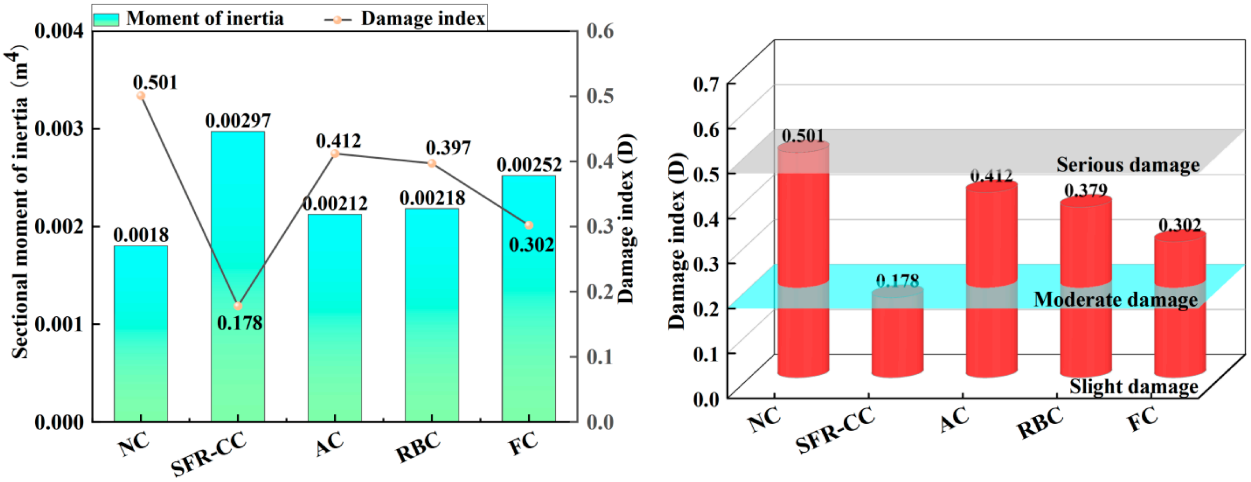

(**a**) Remaining sectional moment of inertia (**b**) Damage level

Figure 17. Classification of damage levels for different concrete reinforcement schemes.

6.2.2. Prediction of Damage Level

To further elucidate the effects of varying explosive charges and blast-facing reinforcement of SFR-CC layers on the disturbance degree of RC slabs, numerical simulations were performed. These simulations evaluated the protective performance under the orthogonal interaction of six explosive charge levels (1 kg, 2 kg, 4 kg, 6 kg, 8 kg, and 9 kg) and four protective layer thicknesses (70 mm, 100 mm, 130 mm, and 160 mm) within the SFR-CC scheme. The disturbance classification of the RC plates and the critical prediction curves for damage grades under different explosive charges and SFR-CC layer thicknesses can be observed in Figure 18. Based on the damage index of reinforced concrete slabs, the prediction curves dividing damage grades of protected reinforced concrete slabs were fitted. Such curves can be used to rapidly evaluate the damage degree of protected reinforced concrete slabs subjected to different charge masses and protective layer thicknesses under contact explosion with identical loading parameters. As presented in Figure 18, the residual sectional moment of inertia of protected reinforced concrete slabs varies significantly with different reinforcement schemes, explosive charges, and SFR-CC protective layer thicknesses. Based on this, damage grades were defined according to the damage coefficients, and critical prediction curves for the damage grades of RC slabs were subsequently derived.

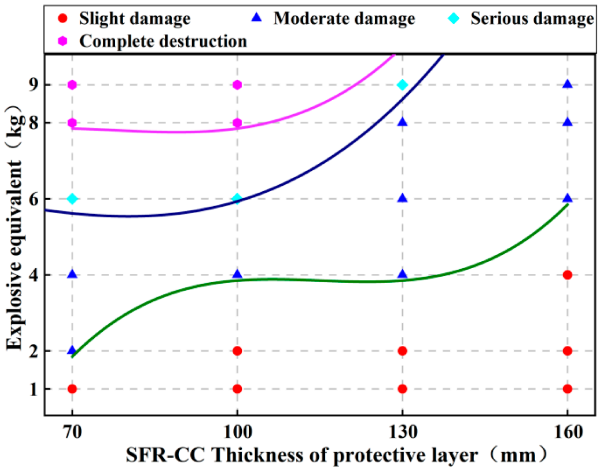

Figure 18. Damage prediction curve of SFR-CC protective layer reinforcement scheme.

The critical prediction curves corresponding to the damage grade transitions of protected reinforced concrete slabs—from mild damage to moderate damage, moderate damage to severe damage, and severe damage to complete destruction—under blast-facing reinforcement schemes with varying explosive charges and SFR-CC layer thicknesses can be observed in Figure 18. The expressions for these critical prediction curves are provided below:

$$\begin{cases} W = 0.315T - 0.0042T^2 + 1.78 \times 10^{-5}T^3 + 0.01, (70\text{ mm} \le T \le 160\text{ mm}), R^2 = 0.976 \\ W = 0.0168T - 0.0011T^2 + 7.907 \times 10^{-6}T^3 + 6.903, (70\text{ mm} \le T \le 160\text{ mm}), R^2 = 0.985 \\ W = 0.974T - 0.0085T^2 + 2.469 \times 10^{-5}T^3 - 33.063, (70\text{ mm} \le T \le 160\text{ mm}), R^2 = 0.988 \end{cases} \quad (8)$$

In the formula above, W is the mass of the explosive, kg; T is the thickness of the SFR-CC protective layer, mm; R^2 is the correction factor.

The damage prediction surfaces, derived from the disturbance coefficients of protected RC slabs subjected to contact detonation loading with varying explosive charges and SFR-CC player thicknesses, are presented in Figure 19. Different protective conditions were established based on the orthogonal interaction between the protective layer thickness (70 mm $\le$ T $\le$ 160 mm, abscissa) and the explosive equivalent weight (1 kg $\le$ W $\le$ 9 kg, ordinate). Finite element analyses were carried out to obtain the spatial distribution of the damage coefficients for the protected RC slabs. These damage coefficients were then fitted to develop a spatial prediction surface that relates the damage coefficient to the explosive equivalent weight and protective layer thickness. The fitted surfaces demonstrated a high degree of agreement with the spatial distribution of the damage coefficients, achieving a coefficient of determination (R^2) of 0.975. This result indicates that the proposed empirical formula effectively characterizes the relationship among explosive equivalent weight, SFR-CC layer thickness, and the disturbance coefficient of RC plate under contact explosions. Consequently, this approach enables quick assessment of damage extent of protected RC slabs strengthened with various schemes of different explosive charges and SFR-CC protective layer thicknesses under contact explosions with identical loading parameters. The empirical formula for the prediction surfaces is provided as follows:

$$D = 0.078T + 0.003W + 0.0073T^2 - 1.05 \times 10^{-5}W^2 - 6.54 \times 10^{-4}TW - 0.059, R^2 = 0.975 \quad (9)$$

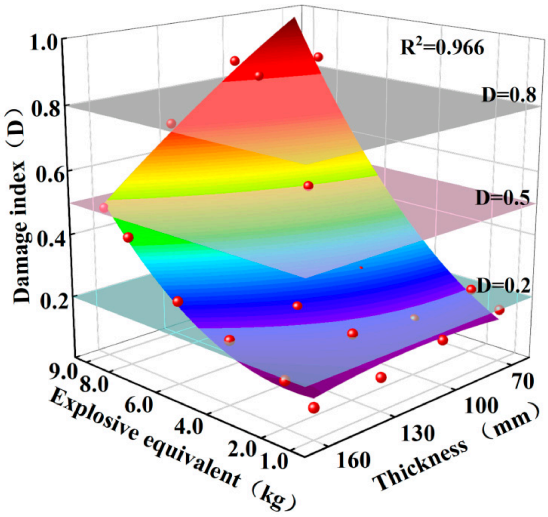

Figure 19. Damage prediction surface of SFR-CC protective layer reinforcement scheme.

7. Conclusions

In this study, the LS-DYNA R11.1 numerical simulation software was adopted to simulate and analyze the damage evolution of RC plate strengthened on the blast-receiving surface with various concrete layers under contact explosion loading. It examined the impact of blast-facing reinforcement combined with different concrete layers on structural anti-explosion capacity, offering a theoretical foundation for further investigations. The primary conclusions are summarized below:

(1) The ALE method was employed to develop a numerical model, and its computed outputs were contrasted against test measurements to validate the method's effectiveness. The findings demonstrate that the proposed approach accurately reproduces the damage patterns observed in reinforced concrete slabs with blast-facing reinforcement across various concrete protective layer configurations under contact detonation loading.

(2) The present investigation examines the attenuation of shock waves, energy absorption capacity, and damage mitigation effects in RC plate retrofitted with diverse types of concrete layers. It also analyzes shock wave propagation characteristics, peak pressures at measurement points, and the total energy absorbed by the protective layers under different concrete reinforcement schemes. Notably, the peak pressure at measurement points for the SFR-CC reinforcement scheme (T-1) is reduced by up to 59%, representing a decrease of as much as 46.6% relative to alternative concrete overlay configurations. Furthermore, the total energy absorbed by the SFR-CC layer (5.13 kJ) is significantly higher than that absorbed by the NC protective layer (3.35 kJ), indicating a substantial improvement in energy absorption efficiency.

(3) The process of damage propagation, evolution, and the underlying damage mechanisms in protected reinforced concrete slabs with blast-facing reinforcement and various concrete protective layers were analyzed. It was found that, compared to the NC protective layer reinforcement scheme, all other concrete layer reinforcement schemes alleviated the damage severity of the protected RC slabs. Among all schemes, the damage suppression performance of the strengthening scheme with SFR-CC layers (T-1) achieves superior protective capacity under the numerical working conditions specified in this paper.

(4) The anti-blast performance of diverse blast-facing concrete layer schemes on reinforced concrete slabs were evaluated. Specifically, the maximum support rotation angle of the RC plate protected by the SFR-CC reinforcement scheme (T-1) is 0.20°, representing a

maximum reduction of 57.5% compared to other concrete layer schemes. This verifies that the SFR-CC concrete layer reinforcement scheme results in the least destruction to the protected reinforced concrete slabs and demonstrates the optimal protective performance under the adopted simulation parameters.

(5) The damage coefficients were calculated based on the residual sectional moment of inertia of reinforced concrete slabs protected with blast-facing strengthening, incorporating various concrete protective layer configurations. Specifically, the damage coefficient for slabs reinforced with the SFR-CC protective layer (T-1) was 0.178. Compared to the NC protective layer reinforcement scheme, this represented a transition in damage grade from severe to mild. Furthermore, the damage coefficient was reduced by up to 41.1% relative to other concrete protective layer reinforcement schemes, indicating a substantial reduction in the extent of destruction.

(6) In accordance with the predefined damage grading criteria, damage grade prediction curves were established for protected RC slabs subjected to the combined effects of varying explosive equivalent weights and protective layer thicknesses. Additionally, an empirical formula was derived to describe the relationship among the damage coefficient, explosive charge, and protective layer thickness. This formula facilitates the rapid assessment of damage severity in protected RC slabs under contact detonation loading with different explosive charges and SFR-CC protective layer thicknesses.

Author Contributions: K.C. and M.M.: Investigation, Formal analysis, Supervision, Resources; S.D.: Data curation, Methodology, Writing—original draft; J.Z.: Supervision, Investigation, Validation, Resources; R.S.: Investigation, Validation, Resources, Formal analysis; K.C.: Conceptualization, Methodology, Writing—review and editing; C.Z.: Data curation, Methodology, Supervision, Resources. All authors have read and agreed to the published version of the manuscript.

Funding: research is supported by Natural Science Foundation of Henan (No. 252300421557, No. 252300421338), Natural Science Foundation of China (No. 51779168), Natural Science Foundation of China (No. 51979188).

Data Availability Statement: The data presented in this study are available on request from the corresponding author due to the large volume of simulation results for each numerical operating condition in this study, the storage capacity of calculation files for a single operating condition can reach 15 GB. The total capacity of all model input files, material parameter files, and complete output data is close to 6 GB. Due to the file upload size limitation of the journal submission system, it is not possible to directly upload all datasets in the manuscript. Therefore, if there is a need for relevant model files, calculation parameters, and simulation results for academic exchange and secondary analysis in the future, they can be obtained by contacting the corresponding author.

Conflicts of Interest: Author Jinlei Zheng was employed by the company Henan Railway Construction and Investment Group Limited Company and Henan New Infrastructure of Railway Construction Investment Limited Company. Ran Song was employed by the company China Railway Design Corporation. The remaining authors declare that the research was conducted in the absence of any commercial or financial relationships that could be construed as a potential conflict of interest.

References

1. Berthelsen, M.; Hansen, M.B.; Nissen, A.; Nielsen, M.B.; Knardahl, S.; Heir, T. The Impact of a Workplace Terrorist Attack on the Psychosocial Work Environment: A Longitudinal Study from Pre- to Post-disaster. *Front. Public Health* **2021**, *9*, 708260. [CrossRef] [PubMed]
2. Okumura, T. Fifteen Years since the Tokyo Subway Attack and Development of Chemical, Biological, Radiological, Nuclear, or Explosive Terrorist Countermeasures in Japan. *Prehospital Disaster Med.* **2009**, *24*, s157.
3. Carbonelli, M.; Quaranta, R.; Gaudio, P.; Giovanni, D.; Xerri, G.P.; Malizia, A.; Gratta, L. Building risk assessment methodology for explosive and non-conventional terrorist attacks. *Eur. Phys. J. Plus* **2024**, *139*, 669. [CrossRef]

4. Beazant, G. Exploding market: Fear of terrorism has created a sudden surge in programs modelling the results of attacks and blasts on buildings. *Prof. Eng.* **2005**, *18*, 43.
5. Yuan, S.; Hao, H.; Zong, Z.; Li, J. A study of RC bridge columns under contact explosion. *Int. J. Impact Eng.* **2017**, *109*, 378–390. [CrossRef]
6. Chiquito, M.; López, L.M.; Castedo, R.; Santos, P.A.; Caldentey, P.A. Full-Scale Field Tests on Concrete Slabs Subjected to Close-In Blast Loads. *Buildings* **2023**, *13*, 2068.
7. Jahromi, H.Z.; Izzuddin, B.A.; Nethercot, D.A.; Donahue, S.; Hadjioannou, M.; Williamson, E.B.; Engelhardt, M.; Stevens, D.; Marchand, K.; Waggoner, M. Robustness Assessment of Building Structures under Explosion. *Buildings* **2012**, *2*, 497–518. [CrossRef]
8. Rampini, M.C.; Zani, G.; Colombo, M.; di Prisco, M. Advancing construction techniques: Textile reinforced concrete shells and high-performance fiber-reinforced concrete beams for partially prefabricated elevated slabs. *Structures* **2024**, *70*, 107710. [CrossRef]
9. Wang, Z.; Chen, W.; Huang, Z.; Hao, H. Numerical study on perforation damage and fragmentation of reinforced concrete slab under close-in explosion. *Eng. Fail. Anal.* **2024**, *158*, 107985. [CrossRef]
10. Yu, J.; Yu, X.F.; Tang, J.H.; Deng, Y.J. Local damage of precast concrete columns with grout sleeve connections under contact detonation. *Eng. Struct.* **2022**, *265*, 114499. [CrossRef]
11. Wang, R.; Zhou, G.; Zuo, X. Test and Numerical Study on Blast Resistance of Main Girders Coated with Polyurea in Self-Anchored Suspension Bridges. *Appl. Sci.* **2024**, *14*, 9280. [CrossRef]
12. Zhang, R.; Ju, J.; Ye, X.; Gao, F.; Zou, T.; Huang, W.; Dong, Q. Study on the effect of mechanical and damping properties of polyurea on blast mitigation performance and protection mechanism. *Prog. Org. Coat.* **2024**, *197*, 108783. [CrossRef]
13. Jia, X.; Zeng, H.; Gao, Q.; Huang, Z.; Bai, X.; Zhao, Y.; Zhao, H. Impact resistance and structural optimization of POZD coated composite plates. *Int. J. Crashworthiness* **2023**, *28*, 601–615.
14. Shi, J.J.; Huang, X.Z.; Ma, B.; Jia, X.; Huang, Z.R. Study on the self-sealing properties of POZD coated aluminium composite structure penetrated by projectiles. *J. Phys. Conf. Ser.* **2024**, *2891*, 072016. [CrossRef]
15. Wang, W.; Wei, G.; Wang, X.; Yang, J. Structural damage assessment of RC slab strengthened with POZD coated steel plate under contact explosion. *Structures* **2023**, *48*, 31–39.
16. Yu, X.; Wang, A.; Wang, M.; Li, T.; Wei, G.; Shao, Z. Design of continuously radial density-graded aluminum foam with unidirectional and bidirectional and study on blast resistance of sandwich tube. *J. Sandw. Struct. Mater.* **2025**, *27*, 345–373.
17. Li, T.; Zhao, J.; Yu, X.; Wang, A.; Chen, S.; Ni, N.; Shao, Z. Dynamic Response of Gradient Aluminum Foam Sandwich Tubes under External Explosive Loads. *Materials* **2024**, *17*, 4501. [CrossRef] [PubMed]
18. Wu, W.; Liu, Y.; Yan, J.; Wang, B.; Bai, F.; Huang, F. Blast performance of polyurethane foam-filled auxetic honeycomb sandwich beams. *Compos. Struct.* **2024**, *338*, 118104. [CrossRef]
19. Wu, J.; Liu, Z.; Yu, J.; Xu, S. Experimental and numerical investigation of normal reinforced concrete panel strengthened with polyurea under near-field explosion. *J. Build. Eng.* **2022**, *46*, 103763. [CrossRef]
20. Huang, W.; Zhang, R.; Wang, X.; Lyu, P.; Ju, J.; Gao, F.; Yan, S. Study of Blast Mitigation Performance and Fracture Mechanism of Polyurea under Contact Explosion. *Polymers* **2022**, *14*, 3458. [CrossRef] [PubMed]
21. Wang, W.; Zhang, C.; Yang, G. Anti-explosion Performance of a New Type of Polyurea-Coated Corrugated Steel Plate Reinforced Concrete Slab. *Int. J. Concr. Struct. Mater.* **2024**, *18*, 42. [CrossRef]
22. Li, X.; Zhang, G.; Liang, M.; Tian, Z. Research on Blast Resistance of the Cylinder with Aluminium Foam under Internal Explosive Load. *J. Phys. Conf. Ser.* **2022**, *2202*, 012024. [CrossRef]
23. Tang, C.; Cao, K.; Zhao, Y. Explosion proof mechanism and damage level prediction of underwater contact explosion of steel fiber reinforced porous concrete slab. *Explos. Impact* **2025**, *45*, 60–75.
24. Nguyen, T.T.; Bui, H.H.; Ngo, D.T.; Nguyen, G.D. Experimental and numerical investigation of influence of air-voids on the compressive behaviour of foamed concrete. *Mater. Des.* **2017**, *130*, 103–119. [CrossRef]
25. Wang, G.; Deng, Z.; Xu, H.; Wang, D.; Lu, Z. Application of Foamed Concrete Backfill in Improving Antiexplosion Performance of Buried Pipelines. *J. Mater. Civ. Eng.* **2021**, *33*, 04021052. [CrossRef]
26. Jiang, N.; Ge, Z.; Wang, Z.; Gao, T.; Zhang, H.; Ling, Y.; Šavija, B. Size effect on compressive strength of foamed concrete: Experimental and numerical studies. *Mater. Des.* **2024**, *240*, 112841. [CrossRef]
27. Ren, D.; Wu, P.; Yang, H.; Xu, J.; Wang, Z.; Huang, Y.; Chen, X.; Kong, L. Mesoscopic evaluation of dynamic water scour resistance of basalt fiber-reinforced porous asphalt concrete using CT scanning technology. *Constr. Build. Mater.* **2025**, *465*, 140186. [CrossRef]
28. Bao, L.; He, M.; Wang, S.; Wu, X. Study on the Effect of Asphalt Static Conditions on the Tensile Properties of Acidic Aggregate Hydraulic Asphalt Concrete. *Materials* **2024**, *17*, 2627. [CrossRef] [PubMed]
29. Huang, X.; Yue, T.; Zhang, J.; Zhang, J. Experimental Research on the Impact Resistance Mechanical Properties and Damage Mechanism of Rubberized Concrete under Freeze–Thaw Cycling. *J. Compos. Sci.* **2024**, *8*, 87. [CrossRef]

30. Xiong, Z.; Fang, Z.; Feng, W.; Liu, F.; Yang, F.; Li, L. Review of dynamic behaviour of rubberised concrete at material and member levels. *J. Build. Eng.* **2021**, *38*, 102237. [CrossRef]
31. Cao, K.; Tang, C.; Zhao, Y.; Huang, H.; Bai, W.; Zhang, L. Evaluation of the performance and effect of steel fiber reinforced cellular concrete for underwater blast protection under contact explosion loading. *Eng. Fract. Mech.* **2025**, *313*, 110668. [CrossRef]
32. Shang, W.; Huang, Z.; Zu, X.; Xiao, Q.; Jia, X. Influence Mechanism of Foamed Concrete Coating Thickness on the Blast Resistance of RC Walls. *Materials* **2022**, *15*, 5473. [CrossRef] [PubMed]
33. Zhao, Z.; Mei, Y.; Zhang, A.; Zeng, C.; Li, F.; Huang, L.; Xu, H. Research on Impact Compression Strength and Explosion Resistance of Layered Gradient Rubber Concrete in Underground Engineering. *Iran. J. Sci. Technol. Trans. Civ. Eng.* **2024**, *49*, 2427–2444. [CrossRef]
34. Wu, J.; Li, L.; Du, X.; Liu, X. Numerical Study on the Asphalt Concrete Structure for Blast and Impact Load Using the Karagozian and Case Concrete Model. *Appl. Sci.* **2017**, *7*, 202. [CrossRef]
35. Guo, S.; Liu, F.; Chen, J.; Yang, J.; He, X. Dynamic response and blast resistance mechanism of polyurea coating on RC slab during contact explosions. *Constr. Build. Mater.* **2024**, *411*, 134271. [CrossRef]
36. Zhao, C.; He, K.; Zhi, L.; Lu, X.; Pan, R.; Gautam, A.; Wang, J.; Li, X. Blast behavior of steel-concrete-steel sandwich panel: Experiment and numerical simulation. *Eng. Struct.* **2021**, *246*, 112998.
37. Malvar, L.J. Review of static and dynamic properties of steel reinforcing bars. *ACI Mater. J.* **1998**, *95*, 609–616. [CrossRef]
38. Cao, K.; Fu, Q.; Zhang, J.; Huang, J.; Tang, C.; Ma, W. Study on the protection mechanism and damage grade prediction of different corrugated steel–concrete composite structures under underwater contact explosion. *Ocean Eng.* **2024**, *292*, 116520.
39. Zhao, C.; Chen, J. Damage mechanism and mode of square reinforced concrete slab subjected to blast loading. *Theor. Appl. Fract. Mech.* **2013**, *63*, 54–62. [CrossRef]
40. Liu, A.; Wang, G.; Lu, W.; Chen, M.; Yan, P. Blast resistance of concrete gravity dams subjected to underwater contact explosion with different protective measures. *Eng. Struct.* **2024**, *316*, 118622. [CrossRef]
41. Liu, Y.; Zhou, R.; Fireha, A.; Chen, H.M.; Wang, W.; Wang, J. Numerical assessment of impact resistance of rubberized metaconcrete with the modified K&C model. *J. Build. Eng.* **2025**, *101*, 111866. [CrossRef]
42. Liu, X.; Chen, J.; Xu, Q. Numerical analysis of explosion load and study on blast resistance performance of concrete gravity dam. *J. Comput. Mech.* **2018**, *35*, 174–181.
43. *UFC 3-340-02*; Structures to Resist the Effects of Accidental Explosion. U.S. Department of Defense: Washington, DC, USA, 2008.
44. Yan, Q.; Zhao, K.; Li, S.; Li, C. Failure modes and damage assessment of box girders under explosive loads. *J. Beijing Inst. Technol.* **2022**, *48*, 961–967. (In Chinese)